hydrogen

MDPI

Article

Comparative Analysis of Control Strategies for Green Hydrogen Production in Off-Grid Photovoltaic Systems: Regulation, Robustness, and Techno-Economic Implications

Ricardo Flores [1], Antonio Sánchez-Squella [1], Aldo Barrueto [1,*], Dhruv Shah [2], Fernando Yanine [3] and Rodrigo Barraza [4]

[1] Department of Electrical Engineering, Universidad Técnica Federico Santa María, Santiago 8320000, Chile; ricardo.floresr@usm.cl (R.F.); antonio.sanchez@usm.cl (A.S.-S.)
[2] Corporación Instituto Nacional del Hidrógeno, Santiago 8320000, Chile; dhruv.shah@inh2.cl
[3] Faculty of Engineering, Universidad Finis Terrae, Santiago 7501015, Chile; fyanine@uft.cl
[4] Center for Energy Transition, Faculty of Engineering and Sciences, Universidad Adolfo Ibáñez, Santiago 7941169, Chile; rodrigo.barraza@uai.cl
* Correspondence: aldo.barrueto@usm.cl

Abstract

Off-grid green hydrogen production couples photovoltaic generation, battery storage, and proton exchange membrane (PEM) electrolysis on a shared DC bus. Advanced nonlinear controllers are routinely proposed for this coupling, yet rarely compared against simpler baselines under a framework covering aging and economics, and rarely decomposed to show which element of the design produces the benefit. We compare a PI cascade, input–output feedback linearization (IO-FL), and interconnection and damping assignment passivity-based control (IDA-PBC) on a seven-state averaged model of a photovoltaic, battery, and PEM electrolyzer system sized for northern Chile, together with three ablation variants: a PI cascade with a model-based power-balance feed-forward, IO-FL with integral action, and IDA-PBC retuned to the common damping ratio. All are tuned to the same closed-loop bandwidth and tested under cloud drop-outs, 200 paired Monte Carlo runs with ±20–30% plant perturbations, a second Monte Carlo set in which the controllers operate with nominal models, measurement bias and sensor errors, a representative day with supervisory start/stop operation, published degradation models, and a levelized cost of hydrogen (LCOH) analysis. On the slow bus-voltage manifold, the IDA-PBC law coincides with IO-FL augmented by an integrator, and the regulation benefit of both is explained by the power-balance feed-forward: adding that single term to the PI cascade lowers the peak DC bus deviation from 4.57% to 0.65%, below the 0.88% of IDA-PBC, and it does so in every Monte Carlo realization. When the controllers operate with nominal models and corrupted measurements, the four variants that combine the feed-forward with integral action become indistinguishable and keep the ±2% target in every realization, while the canonical IO-FL misses it in three realizations out of four. The three design routes, however, are indistinguishable on cost and component life: under supervisory operation, the battery throughput and the PEM start/stop count are set by the energy management layer, and the six controllers give the same LCOH to the fourth decimal place. For the architecture, supervisory strategy, and operating scenarios investigated here, the case for a particular control law rests on regulation quality, robustness to model error, and the availability of a stability certificate, not on longer component life or cheaper hydrogen.

Check for updates

Academic Editor: Sergio Alberto Obregón Alfaro

Received: 7 September 2026
Revised: 26 October 2026
Accepted: 28 October 2026
Published: 1 November 2026

Copyright: © 2026 by the authors. Licensee MDPI, Basel, Switzerland. This article is an open access article distributed under the terms and conditions of the Creative Commons Attribution (CC BY) license.

Keywords: green hydrogen production; PEM electrolyzer; passivity-based control; degradation; DC microgrid; levelized cost of hydrogen

1. Introduction

Green hydrogen, produced through water electrolysis powered by renewable energy, has become a central vector for the decarbonization of transportation, power generation, and industry [1,2]. Photovoltaic (PV) production pathways are particularly attractive in regions of exceptionally high irradiance such as the Atacama Desert in northern Chile, which exhibits one of the highest global horizontal irradiance levels worldwide [3], and benefit from the sustained cost reduction that has made utility-scale solar PV the most cost-competitive new electricity source [4].

Continuous hydrogen production under intermittent irradiance requires energy storage [5]. Batteries are the most mature option for covering short-term fluctuations: they store surplus solar energy and release it when irradiance drops, improving the utilization factor of the electrolyzer [6]. Their role is critical in off-grid installations, where generation and consumption rely exclusively on local resources, and surpluses cannot be exchanged with a grid [7]. Batteries also protect the electrolyzer: proton exchange membrane (PEM) stacks degrade under abrupt current and voltage fluctuations, with reported voltage degradation rates of 20–50 μV/h driven mainly by frequent ON/OFF cycling, catalyst dissolution, and electrode delamination [8,9]. Frensch et al. [10] demonstrated that the degradation rate scales linearly with current ripple density and cycling frequency, and Rakousky et al. [11] characterized the role of fluctuating power profiles in membrane degradation. A battery buffer that smooths these fluctuations can therefore extend electrolyzer life and reduce replacement and maintenance costs [12].

The battery itself degrades with depth of discharge, temperature, cycling throughput, and average state of charge [13]. For lithium iron phosphate (LFP) chemistries, increasingly adopted in stationary storage, Naumann et al. [14,15] developed and experimentally validated calendar and cycle aging models as functions of these stress factors. Component durability and replacement frequency are, in turn, critical variables for project profitability [16]: for the Atacama context, utility-scale techno-economic studies report levelized costs of hydrogen (LCOH) between 2.12 USD/kg for direct solar–PEM coupling [17] and 3.67–4.69 USD/kg for various configurations [18], with installed PEM electrolyzer CAPEX of 1500–2500 USD/kW [19] and small stationary battery costs of 300–500 USD/kWh [20]. Control and energy-management design must therefore address the coupled nonlinear dynamics of PV generation, battery storage, and electrolysis [21–23], together with their degradation and cost implications.

A broad family of advanced control methods has been proposed for this class of systems. Model predictive control (MPC) anticipates system behavior through dynamic models and has shown improved efficiency and reduced settling times in hydrogen-supported microgrids [24,25], at the cost of detailed models and computational capacity that can limit remote deployment. Fuzzy logic controllers reduce current ripple without requiring explicit models [26], but their performance may deteriorate under conditions not considered at design time. Sliding-mode control offers strong robustness to disturbances and parameter variations of up to 30% [27], with recent hardware-in-the-loop validation of higher-order variants [28], although chattering remains a concern for electrolyzer-grade current quality. Adaptive and learning-based hierarchical schemes adjust to changing conditions and gradual component degradation [29,30], at the price of computationally intensive training or communication infrastructure.

Simpler strategies remain competitive. The proportional–integral (PI) cascade is widely used for its simplicity, low computational demand, and solid steady-state performance [26] but degrades under fast irradiance transients. Feedback linearization (FL) transforms the nonlinear converter dynamics into linear equivalents and has achieved precise disturbance rejection in electrolyzer-feeding converters [31], although its effectiveness depends on model quality. Interconnection and damping assignment passivity-based control (IDA-PBC) [32] exploits the port-controlled Hamiltonian structure of the physical dynamics to guarantee stability without linearization and has been successfully applied to DC–DC converters and isolated networks with storage [33]; unlike two-stage stochastic optimization [34] or MPC-based energy management with hydrogen storage [35], it directly addresses the closed-loop dynamic control of the converters while retaining a complexity compatible with real-time implementation and hierarchical supervision [36]. Our previous work [37] demonstrated an efficient DC–DC coupling architecture for off-grid green hydrogen production with PEM electrolysis, PV generation, and battery storage, although without a comparative control evaluation or quantitative aging analysis.

Research Gaps and Contributions

Despite this body of work, we are not aware of a study that combines the three elements needed to substantiate the practical case for advanced control in off-grid green hydrogen systems: (i) a side-by-side comparison of multiple controllers under identical conditions and matched tuning specifications; (ii) quantitative aging models for both the battery and electrolyzer; and (iii) statistical robustness analysis coupled with a levelized cost of hydrogen evaluation. The works we have reviewed address one or two of these dimensions at a time. Recent contributions focus on either advanced control without quantitative degradation impact [25,28,31,33], techno-economic analysis without controller comparison [7,17,18], or sizing optimization without dynamic control evaluation [34]. Even the most comprehensive prior assessment of off-grid solar hydrogen [7] applies Monte Carlo uncertainty analysis to input parameters but does not compare control strategies. This gap is relevant because the claim that advanced nonlinear control reduces the lifecycle cost of hydrogen production is, as far as we know, seldom tested quantitatively against simpler alternatives under matched conditions and well-dimensioned power electronics. A second, more specific gap concerns attribution: comparative studies report that a nonlinear controller outperforms a PI baseline but seldom separate the contribution of the model-based feed-forward that every such controller embeds from that of its structural properties, so the reader cannot tell which part of the design is doing the work.

The present article addresses these gaps through a comparative analysis of three control approaches—PI cascade, input–output feedback linearization (IO-FL), and IDA-PBC—and three ablation variants, applied to the converter-level control of an autonomous system with solar panels, LFP battery storage, and PEM-based hydrogen production. The controllers regulate the DC bus, the PV operating point, and the converter currents; the electrolyzer set-point, start/stop decisions, and state-of-charge management belong to a supervisory layer that is common to all of them. The main contributions are:

1. A full seven-state nonlinear dynamic model of the off-grid PV–battery–PEM system that captures photovoltaic generation with maximum power point tracking, battery state-of-charge dynamics, electrolyzer thermal behavior, and averaged converter dynamics, providing a unified framework for the three control strategies tuned to matched bandwidth specifications.
2. A quantitative degradation assessment using two post-processor models validated by their authors on commercial cells and stacks: the Naumann cycle/calendar aging model for LFP cells [14,15] and the Frensch voltage degradation model for PEM

stacks [10], applied as published and identically to all controllers and to multiple operating scenarios.

3. A Monte Carlo statistical analysis with paired hypothesis testing that establishes the significance of the observed performance differences under randomized parameter perturbations (±20–30% in converter inductances, capacitances, and resistances; ±5% in the battery and electrolyzer electrochemical parameters), addressing controller sensitivity to model uncertainty.
4. A levelized cost of hydrogen analysis with fully referenced parameters (IRENA, DOE, IEA, and PNNL benchmarks) and sensitivity to capital expenditure, weighted average cost of capital, project horizon, and operating hours, allowing transparent comparison with the Atacama benchmarks reported by Gallardo et al. [18] and Armijo and Philibert [17].
5. A decomposition of where the regulation benefit of nonlinear control comes from. On the slow bus-voltage manifold, the IDA-PBC law is shown, analytically and numerically, to coincide with IO-FL augmented by an integrator, and an ablation study (PI with a power-balance feed-forward, IO-FL with integral action, IDA-PBC retuned to $\zeta = 0.707$) shows that the model-based feed-forward explains the 5–7-fold reduction in the peak bus deviation, and the integrator explains the accumulated-error ranking. A PI cascade with that feed-forward reaches 0.65% peak deviation, below IDA-PBC, in every one of 200 perturbed plants.
6. A robustness assessment in which the controllers operate with nominal models while the plant, the irradiance and temperature measurements, the stack and battery models used by the controllers, and the voltage and current sensors are perturbed, showing which of the six variants keep the ±2% regulation target under realistic model error and which do not.
7. A demonstration that, for the investigated battery-buffered architecture operated under a shared supervisory strategy, component life and LCOH are governed by the architecture and the supervisory layer rather than by the converter-level controller: under a representative day with PV-following set-point and start/stop events, the battery throughput and the PEM cycling count are identical across controllers, and the LCOH coincides across controllers to the fourth decimal in all tested sensitivity scenarios, including battery sizing. This changes how the case for IDA-PBC should be made in systems of this kind and gives concrete guidance for choosing a controller in such deployments.

The remainder of this paper is organized as follows. Section 2 presents the system architecture, the component models, the three controllers tuned to matched closed-loop specifications, the degradation models, and the simulation, statistical, and economic methodology. Section 3 reports the deterministic stress results, the Monte Carlo robustness analysis, the component aging assessment, and the LCOH analysis. Section 4 discusses the implications of the findings, and Section 5 concludes this paper.

2. Methodology

This section presents the system architecture, the component models, the three control strategies, the degradation models, and the simulation, statistical, and economic methodology. Compared with our previous study [37], the system operates at a 400 V DC link and includes physics-based dynamic models of the photovoltaic array, the lithium iron phosphate (LFP) battery, and the proton exchange membrane (PEM) electrolyzer; the resulting seven-state averaged plant provides a common reference for the three controllers, which are tuned to matched closed-loop bandwidth specifications to enable a fair comparison.

2.1. System Architecture

Figure 1 shows the schematic configuration of the off-grid hydrogen generation system. It consists of three subsystems coupled to a common DC bus through dedicated DC–DC converters: (i) a photovoltaic array connected through a boost converter operating under maximum power point tracking (MPPT); (ii) an LFP battery energy storage system connected through a bidirectional buck-boost converter; and (iii) a PEM electrolyzer connected through a buck converter. The DC bus is stabilized by a capacitor C_{bus} that maintains the reference voltage V^*_{bus} and acts as the common point of energy exchange between sources, storage, and load.

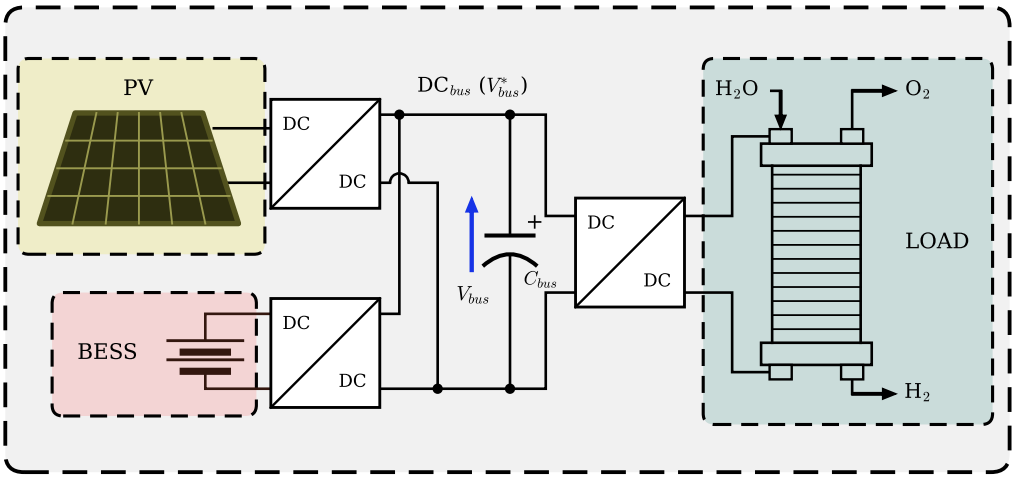


Figure 1. Proposed connection scheme for the off-grid green hydrogen production system.

Compared to the original 100 V configuration of our previous study [37], the bus voltage has been raised to 400 V to align with typical industrial PEM stack voltage ranges and to reduce conduction losses. The nominal ratings, summarized in Table 1, correspond to a small off-grid hydrogen production unit for remote installations in the Atacama Desert.

Table 1. Nominal system parameters.

Parameter	Symbol	Value
PV array peak power	P_{pv}	4.8 kWp
PV array MPP voltage (STC)	$V_{pv,mpp}$	249 V
Battery nominal energy	E_{bat}	10.24 kWh
Battery nominal voltage (64S)	$V_{bat,n}$	204.8 V
Battery nominal capacity	Q_{nom}	50 Ah
PEM electrolyzer rated power	P_{el}	4 kW
PEM stack cells in series	N_{cells}	50
PEM active area per cell	A_{cell}	100 cm^2
PEM thermal capacitance	C_{th}	5000 J/K
DC bus reference voltage	V^*_{bus}	400 V
DC bus capacitance	C_{bus}	2200 µF
PV converter inductance	L_{pv}	2 mH
PV converter input capacitance	C_{pv}	220 µF
Battery converter inductance	L_{bat}	1 mH
Electrolyzer converter inductance	L_{el}	2 mH
Series resistance (all inductors)	R_L	0.05 Ω
Inner-loop bandwidth	ω_{inner}	1000 rad/s
Outer-loop bandwidth	ω_{outer}	100 rad/s
Damping ratio (current and voltage loops)	ζ	0.707
Switching frequency	f_{sw}	20 kHz

2.2. Photovoltaic Generation Subsystem

The photovoltaic array is modeled following the single-diode five-parameter formulation of Villalva et al. [38], which captures the nonlinear current–voltage relationship as a function of irradiance and temperature:

$$I_{pv} = N_p I_{ph} - N_p I_0 \left[\exp\left(\frac{V_{pv}/N_s + I_{pv} R_s / N_p}{a\, V_T} \right) - 1 \right] - \frac{N_p V_{pv}/N_s + I_{pv} R_s}{R_{sh}} \tag{1}$$

where I_{ph} is the photogenerated current (proportional to irradiance G with temperature correction), I_0 is the diode saturation current, a is the diode ideality factor, V_T is the thermal voltage, R_s and R_{sh} are the series and shunt resistances, and N_s and N_p are the numbers of series and parallel cells. The array configuration is 2 parallel strings of 6 series modules (each module comprising 72 series cells), yielding a nominal MPP voltage of 249 V under standard test conditions. The model parameters are fitted by the iterative procedure of Villalva et al. [38] to reproduce exactly the manufacturer-rated V_{oc}, I_{sc}, and (V_{mpp}, I_{mpp}) points at STC.

The perturb-and-observe MPPT algorithm of Femia et al. [39] is implemented to drive the PV operating voltage toward the maximum power point under varying irradiance:

$$V_{pv}^*(k+1) = V_{pv}^*(k) + \Delta V \cdot \mathrm{sign}\left[\frac{P_{pv}(k) - P_{pv}(k-1)}{V_{pv}(k) - V_{pv}(k-1)} \right] \tag{2}$$

where $P_{pv} = V_{pv}\, I_{pv}$ is the instantaneous photovoltaic array power, with perturbation step $\Delta V = 1.0$ V and sampling period $T_{s,mppt}$ = 10 ms; the reference V_{pv}^* is delivered to the outer-voltage loop of each controller. Unlike our previous study [37], in which the PV converter was abstracted as an ideal current source, the present model retains the full dynamics of the PV-side capacitor and inductor, so the controllers interact with realistic generator dynamics under fast irradiance changes.

2.3. Battery Storage Subsystem

The battery is modeled as a 64-cell LFP series string using the Tremblay–Dessaint formulation [40], which captures the polarization, exponential, and ohmic behavior of the cell voltage:

$$V_{bat} = E_0 - K \cdot \frac{Q}{Q - q(t)}\, q(t) - K \cdot \frac{Q}{Q - q(t)}\, i_{bat}^* + A\, e^{-B\, q(t)} - R_{int}\, i_{bat} \tag{3}$$

where E_0 is the open-circuit constant voltage, K is the polarization constant, $Q = 50$ Ah is the nominal capacity, $q(t) = \int_0^t i_{bat}(\tau)\, d\tau$ is the extracted charge, i_{bat}^* is a low-pass filtered current, A and B are the exponential-zone parameters, and R_{int} is the internal resistance. The pack-level parameters are obtained by scaling cell-level values from the per-cell calibration ($E_{0,cell} = 3.28$ V, $K_{cell} = 1.56 \cdot 10^{-4}$ V/Ah, $A_{cell} = 0.124$ V, $B_{cell} = 0.156$ Ah^{-1}, $R_{cell} = 1.56 \cdot 10^{-3}\ \Omega$) against typical LFP discharge curves; the polarization constant K is one order of magnitude smaller than for conventional NMC/LCO chemistries due to the much flatter LFP voltage profile. The state of charge (SOC) evolves according to

$$\frac{d\,SOC}{dt} = -\frac{i_{bat}(t)}{Q \cdot 3600} \tag{4}$$

with the sign convention $i_{bat} > 0$ during discharge. Both the SOC dynamics and the capacity-dependent voltage profile feed into the aging model presented in Section 2.7.1.

2.4. PEM Electrolyzer Subsystem

The PEM electrolyzer is modeled following García-Valverde et al. [41], with the total cell voltage given as the sum of the reversible potential, the activation overpotentials at both electrodes, the ohmic losses, and the ionic overpotential associated with proton transport across the membrane:

$$V_{el,cell} = E_{rev} + \eta_{act,a} + \eta_{act,c} + \eta_{ohm} + \eta_{ion} \tag{5}$$

where the reversible potential E_{rev} is computed from the Nernst equation with temperature correction, the activation overpotentials follow the Butler–Volmer kinetics at both the anode (α_a = 2.0, $i_{0,a}$ = 10^{-7} A/cm^2) and cathode (α_c = 0.5, $i_{0,c}$ = 10^{-3} A/cm^2), η_{ohm} lumps the electronic resistance of the electrodes and bipolar plates, and η_{ion} accounts for the ionic (proton transport) resistance of the membrane, following the concentration/membrane overpotential treatment emphasized in [41]. All η terms in Equation (5) denote overpotentials expressed in volts, following standard electrochemical notation. The total stack voltage is $V_{el} = N_{cells} \cdot V_{el,cell}$ with N_{cells} = 50 cells in series and an active area A_{cell} = 100 cm^2 per cell, yielding a nominal stack voltage of approximately 96 V at the rated current of 40 A (P_{el} = 4 kW). In the stress and Monte Carlo scenarios, the electrolyzer is operated at the supervisory set-point i_{el}^{*} = 30 A rather than at the rated current; in the representative-day scenario of Section 2.8, the set-point follows the available PV power.

The Faraday efficiency η_F is modeled as a function of current density following Yodwong et al. [42]:

$$\eta_F = \frac{i^2}{f_1 + i^2} f_2 \tag{6}$$

with f_1 = 250 mA^2/cm^4 and f_2 = 0.98.

To capture the slow thermal dynamics relevant to long-term degradation, a lumped-capacitance thermal balance is added:

$$C_{th} \frac{dT_{el}}{dt} = N_{cells}\, i_{el}\, (V_{el,cell} - V_{tn}) - \frac{T_{el} - T_{amb}}{R_{th}} \tag{7}$$

where C_{th} = 5000 J/K is the lumped thermal capacitance, R_{th} = 0.167 K/W is the equivalent thermal resistance to ambient, and V_{tn} = 1.482 V is the thermo-neutral voltage; T_{el} is the electrolyzer stack temperature and T_{amb} is the ambient temperature (298.15 K, 25 °C). The model reproduces the characteristic polarization behavior of PEM electrolyzers. In the stress scenario, the stack starts at 60 °C and, dissipating only to ambient through R_{th}, warms to 92 °C over the 10 min window (mean 79 °C); without active cooling, its steady state at i_{el}^{*} = 30 A would be about 130 °C, which is why the representative-day scenario of Section 2.8 includes the thermal management of the balance of plant. T_{ref} = 60 °C is the reference temperature of the degradation model in Section 2.7.2.

2.5. DC–DC Converters and Averaged Dynamic Model

The three DC–DC converters operate in continuous conduction mode and are described by their state-averaged equations [43]. The seven state variables are the bus voltage V_{bus}; the three inductor currents i_{pv}, i_{bat}, and i_{el}; the PV-side capacitor voltage V_{pv}; the battery state of charge SOC; and the electrolyzer stack temperature T_{el}. The duty cycles of the three converters are u_{pv}, u_{bat}, and u_{el}, taking values in $[0, 1]$.

The averaged dynamic equations are

$$\begin{aligned} C_{bus}\frac{dV_{bus}}{dt} &= (1-u_{pv})\,i_{pv} + u_{bat}\,i_{bat} - u_{el}\,i_{el} \\ L_{pv}\frac{di_{pv}}{dt} &= V_{pv} - (1-u_{pv})\,V_{bus} - R_L\,i_{pv} \\ L_{bat}\frac{di_{bat}}{dt} &= V_{bat} - u_{bat}\,V_{bus} - R_L\,i_{bat} \\ L_{el}\frac{di_{el}}{dt} &= u_{el}\,V_{bus} - V_{el} - R_L\,i_{el} \\ C_{pv}\frac{dV_{pv}}{dt} &= I_{pv}(V_{pv}, G, T_{amb}) - i_{pv} \end{aligned} \tag{8}$$

augmented with the SOC dynamics (4) and the thermal dynamics (7). The sign convention is $i_{bat} > 0$ in discharge, $i_{pv}, i_{el} > 0$ unconditionally. The state-averaging assumption is justified by the wide time-scale separation between the switching frequency (f_{sw} = 20 kHz, period T_{sw} = 50 µs) and the outer-loop control bandwidth (ω_{outer} = 100 rad/s, period ≈ 63 ms), which differ by more than three orders of magnitude. The state-space model (8) corresponds to the averaged power circuit shown in Figure 2, where each converter interfaces its energy device to the common DC bus: the PV array (modeled as the current source I_{pv} with input capacitance C_{pv}) is connected through a boost stage; the LFP battery is interfaced by a bidirectional DC–DC converter; and the PEM electrolyzer is fed from the bus through a buck stage. Each converter inductor carries the lumped series resistance R_L, C_{bus} is the DC-link capacitance, and the duty cycles u_{pv}, u_{bat}, and u_{el} are the averaged control inputs of the three converters.

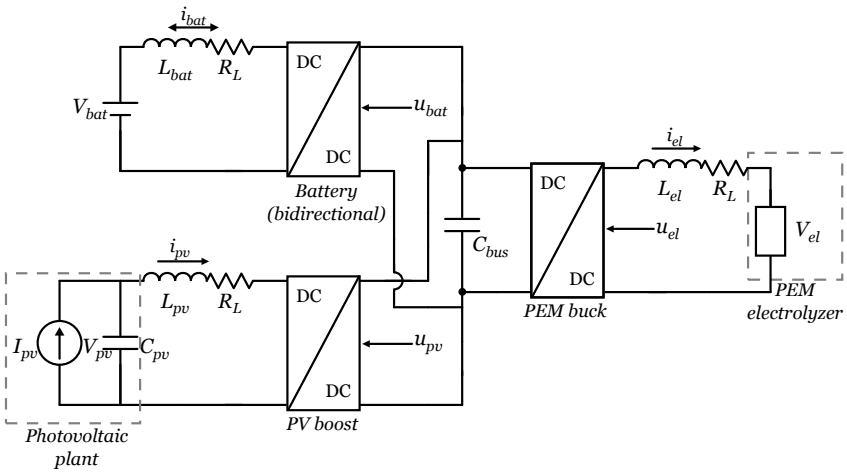


Figure 2. Averaged power circuit of the off-grid PV–battery–PEM electrolyzer system associated with the state-space model in Equation (8). The three DC–DC converters—PV boost, bidirectional battery converter, and PEM buck—share a common 400 V DC bus. The duty cycles u_{pv}, u_{bat}, and u_{el} denote the averaged switching functions of each converter.

2.6. Control Strategies

The three controllers (PI cascade, IO-FL, and IDA-PBC) and the three ablation variants introduced in Section 2.6.4 share identical control objectives:

- Regulate the DC bus voltage at V^*_{bus} = 400 V using the battery as the actuator;
- Track the PV maximum power point through the reference V^*_{pv} delivered by the MPPT algorithm;
- Deliver the reference electrolyzer current i^*_{el} requested by the supervisory level (energy management system).

The controllers compared here are converter-level regulators. They do not decide when the electrolyzer runs, at what set-point, or how the battery state of charge is managed; those decisions are taken by the supervisory layer described in Section 2.8, which is identical for all controllers. Statements about energy management in this paper therefore refer to that layer, not to the control laws under comparison. Bus-voltage regulation is achieved through the battery converter in all three controllers (the electrolyzer is treated as a load that follows its own current reference). All controllers are tuned to the same nominal specifications: inner-current loops with ω_{inner} = 1000 rad/s, outer-voltage loops with ω_{outer} = 100 rad/s, damping ratio ζ = 0.707, yielding a 10:1 time-scale separation.

2.6.1. PI Cascade Control

The PI architecture uses five nested loops with conditional anti-windup integration:

- Two outer-voltage loops: one on V_{pv} that defines i^*_{pv}, and one on V_{bus} that defines i^*_{bat};
- Three inner-current loops that produce the duty cycles u_{pv}, u_{bat}, and u_{el} from the tracking errors of i_{pv}, i_{bat}, and i_{el}, respectively;
- The electrolyzer current reference i^*_{el} is provided directly by the supervisory level and tracked only through the inner-current loop, without an outer-voltage loop.

The block diagram is shown in Figure 3.

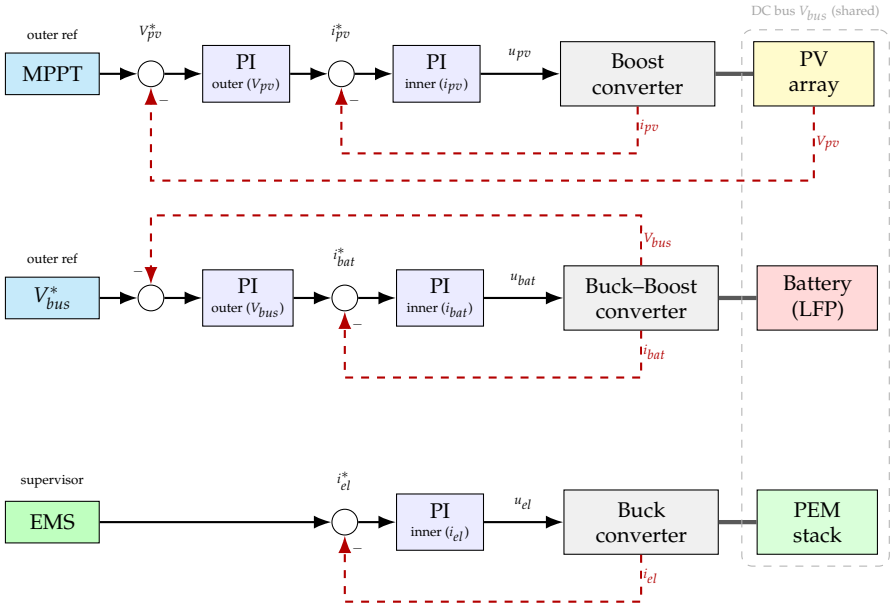


Figure 3. Block diagram of the PI cascade control architecture. Five PI loops with conditional anti-windup integration. Two outer-voltage loops (on V_{pv} and V_{bus}) generate the current references i^*_{pv} and i^*_{bat}; three inner-current loops generate the duty cycles u_{pv}, u_{bat}, and u_{el}. The electrolyzer current reference i^*_{el} is provided directly by the energy management system (EMS). The three power conversion branches share the same DC bus (dashed grouping on the right). The same architecture also defines the structural skeleton of the IO-FL and IDA-PBC controllers presented in Sections 2.6.2 and 2.6.3.

For the design of the PI gains, the plant (8) is linearized around the operating point with equilibrium values $u_{pv,0} = 1 - V_{pv,0}/V_{bus,0}$, $u_{bat,0} = V_{bat,0}/V_{bus,0}$, and $u_{el,0} = V_{el,0}/V_{bus,0}$. Each inner-current loop reduces to a first-order plant of the form $L\,\dot{i} + R_L\,i = K_u\,u$ with $K_u = \pm V_{bus,0}$ depending on converter polarity. Closing the loop with the PI controller

$$G_{PI}(s) = \frac{K_p\,(s\,T_I + 1)}{s\,T_I} \tag{9}$$

and matching the closed-loop response to a second-order prototype yields the analytical gains

$$K_p^{in} = \frac{2\,\zeta\,\omega_{inner}\,L - R_L}{|K_u|}, \qquad K_i^{in} = \frac{\omega_{inner}^2\,L}{|K_u|} \tag{10}$$

For each outer-voltage loop, the inner loop is approximated as a unity gain in the bandwidth of interest (justified by the 10:1 separation), and the resulting first-order voltage plant gives

$$K_p^{out} = \frac{2\,\zeta\,\omega_{outer}\,C}{|K_o|}, \qquad K_i^{out} = \frac{\omega_{outer}^2\,C}{|K_o|} \tag{11}$$

where C is the relevant capacitance (C_{pv} or C_{bus}) and $|K_o|$ is the steady-state gain of the outer loop (1 for V_{pv} and $u_{bat,0}$ for V_{bus}).

Conditional anti-windup integration (Figure 4) is essential: when the electrolyzer is in standby ($i_{el}^* = 0$), the integrator of the inner i_{el} loop would otherwise undergo severe windup within seconds. Padé first-order approximations model actuator delays up to 1 ms.

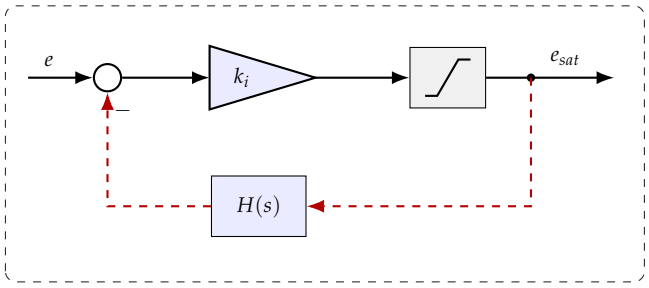


Figure 4. Schematic of the conditional anti-windup PI controller used in each of the five loops.

2.6.2. Input–Output Feedback Linearization

Feedback linearization is based on the work of Isidori [44]. The objective is to design a nonlinear control law that renders the input–output behavior of the system linear. Let a nonlinear SISO system be of the affine form

$$\begin{aligned} \dot{\mathbf{x}} &= \mathbf{f}(\mathbf{x}) + \mathbf{g}(\mathbf{x})\,u \\ y &= h(\mathbf{x}) \end{aligned} \tag{12}$$

with state $\mathbf{x} \in \mathbb{R}^n$, input u, and output y. The relative degree ρ is the smallest integer such that $L_g L_f^{\rho-1} h(x) \neq 0$, where $L_f h$ denotes the Lie derivative of h along f [45,46]. The feedback [47,48]

$$u = \frac{-L_f^{\rho} h(x) + v}{L_g L_f^{\rho-1} h(x)} \tag{13}$$

renders the input–output map a chain of ρ integrators, $y^{(\rho)} = v$; when $\rho < n$, only the input–output relationship is linearized, leading to the input–output feedback linearization (IO-FL) technique.

For the plant (8), three outputs are selected with different relative degrees:

$$\mathbf{h}(x) = \begin{bmatrix} i_{el} \\ V_{pv} \\ V_{bus} \end{bmatrix}, \qquad \boldsymbol{\rho} = \begin{bmatrix} 1 \\ 2 \\ 1 \end{bmatrix} \tag{14}$$

The electrolyzer current i_{el} has relative degree $\rho = 1$ with respect to u_{el} since $\partial \dot{i}_{el} / \partial u_{el} = V_{bus}/L_{el} \neq 0$ for $V_{bus} > 0$ (single-layer feedback linearization). The PV voltage V_{pv} has relative degree $\rho = 2$ with respect to u_{pv}, requiring a cascade structure: the outer loop on

V_{pv} generates i^*_{pv}, and the inner layer linearizes i_{pv} with respect to u_{pv}. The bus voltage V_{bus} has relative degree $\rho = 1$ with respect to u_{bat} (the actuator for V_{bus} regulation), since $\partial \dot{V}_{bus}/\partial u_{bat} = i_{bat}/C_{bus}$; this input gain, however, vanishes whenever the battery current crosses zero, so a direct single-layer inversion would be singular at $i_{bat} = 0$. A cascade structure is therefore adopted by design: the outer loop generates i^*_{bat} and the inner layer linearizes i_{bat} via u_{bat}, whose input gain V_{bus}/L_{bat} remains bounded away from zero. Besides this singularity avoidance, the condition $V_{bus} > 0$ is the only restriction on validity, and it is satisfied throughout normal operation.

Inverting the input–output maps yields the IO-FL control laws. For the single-layer electrolyzer current loop

$$u_{el} = \frac{V_{el} + R_L\, i_{el} + L_{el}\, v_{el}}{V_{bus}}, \qquad v_{el} = k_{el}\,(i^*_{el} - i_{el}) \tag{15}$$

For the cascade PV and battery loops, the outer-voltage layers compute the current references, and the inner-current layers apply exact cancellation:

$$\begin{aligned} i^*_{pv} &= I_{pv} + C_{pv}\, k_{V_{pv}}\,(V_{pv} - V^*_{pv}) \\ i^*_{bat} &= \frac{V_{bus}}{V_{bat}}\left[-(1-u_{pv})\, i_{pv} + u_{el}\, i_{el} - C_{bus}\, k_{V_{bus}}\,(V_{bus} - V^*_{bus})\right] \end{aligned} \tag{16}$$

with inner-layer gains $k_{el} = k_{i_{pv}} = k_{i_{bat}} = \omega_{inner} = 1000$ rad/s and outer-layer gains $k_{V_{pv}} = k_{V_{bus}} = \omega_{outer} = 100$ rad/s, chosen to match the same bandwidths as the PI controller. IO-FL does not include integral action; this is a structural property of the standard formulation that has direct consequences for steady-state accuracy under parametric uncertainty, as discussed in Section 4. An integrator-augmented variant is evaluated alongside the canonical form (Section 2.6.4).

2.6.3. Interconnection and Damping Assignment PBC

Passivity-based control (PBC) achieves stabilization by rendering the closed-loop system passive with respect to a desired storage function with damping injection [49]; IDA-PBC is its natural variant for systems with a port-controlled Hamiltonian (PCH) structure, such as power electronic converters.

The system (12) can be expressed in PCH form as

$$\dot{\mathbf{x}} = [J(x) - R(x)]\,\nabla H(x) + g(x)\,u \tag{17}$$

where $J(x) = -J^T(x)$ is the skew-symmetric interconnection matrix, $R(x) \geq 0$ is the damping matrix, and $H(x)$ is the Hamiltonian (total stored energy). The design selects a desired Hamiltonian $H_d(x)$ with an isolated minimum at the equilibrium x^* and desired matrices $J_d = -J_d^T$, $R_d \geq 0$, and solves the matching PDE [49]

$$g^{\perp}(x)\,\{[J(x) - R(x)]\,\nabla H(x) - [J_d(x) - R_d(x)]\,\nabla H_d(x)\} = 0 \tag{18}$$

with $g^{\perp}$ a full-rank left annihilator of g, so that the closed loop becomes $\dot{x} = [J_d - R_d]\,\nabla H_d$. Taking H_d as a Lyapunov candidate,

$$\dot{H}_d = -[\nabla H_d]^T\, R_d(x)\, \nabla H_d \leq 0 \tag{19}$$

asymptotic stability of x^* follows from LaSalle's invariance principle [50].

In contrast with the 1×1 reduction employed in our previous study [37], the complete port-Hamiltonian representation of the system (8) is derived here. Defining the energy-

conjugate state variables $\mathbf{q} = [q_1, q_2, q_3, q_4, q_5]^T$ with $q_1 = C_{bus}\, V_{bus}$ (charge in bus capacitor), $q_2 = L_{pv}\, i_{pv}$, $q_3 = L_{bat}\, i_{bat}$, $q_4 = L_{el}\, i_{el}$ (fluxes in inductors), and $q_5 = C_{pv}\, V_{pv}$ (charge in PV-side capacitor), the total stored energy (Hamiltonian) is

$$H(q) = \frac{q_1^2}{2C_{bus}} + \frac{q_2^2}{2L_{pv}} + \frac{q_3^2}{2L_{bat}} + \frac{q_4^2}{2L_{el}} + \frac{q_5^2}{2C_{pv}} \tag{20}$$

The gradient is $\nabla H = [V_{bus},\, i_{pv},\, i_{bat},\, i_{el},\, V_{pv}]^T$, recovering the physical voltages and currents as co-energy variables. The PCH form of the plant is

$$\dot{\mathbf{q}} = [J(u) - R]\, \nabla H(\mathbf{q}) + g\, \mathbf{d} \tag{21}$$

with $\mathbf{d} = [V_{bat},\, V_{el},\, I_{pv}(V_{pv}, G, T_{amb})]^T$ the external inputs, and

$$J(u) = \begin{bmatrix} 0 & (1-u_{pv}) & u_{bat} & -u_{el} & 0 \\ -(1-u_{pv}) & 0 & 0 & 0 & 1 \\ -u_{bat} & 0 & 0 & 0 & 0 \\ u_{el} & 0 & 0 & 0 & 0 \\ 0 & -1 & 0 & 0 & 0 \end{bmatrix}, \quad R = R_L\, \mathrm{diag}(0,\, 1,\, 1,\, 1,\, 0), \quad g = \begin{bmatrix} 0 & 0 & 0 \\ 0 & 0 & 0 \\ 1 & 0 & 0 \\ 0 & -1 & 0 \\ 0 & 0 & 1 \end{bmatrix} \tag{22}$$

By construction, $J(u) = -J^T(u)$ for all admissible duty cycles, and $R \geq 0$. This confirms the PCH structure of the full five-state plant and shows that the control action enters through the modulation of the interconnection matrix, not through additive external forces. This generalizes the 1×1 reduction employed in [37], where the full interconnection structure was implicitly collapsed.

A direct IDA-PBC synthesis on the five-state plant would require solving a matching PDE in five variables, which is intractable analytically. We instead exploit the time-scale separation: the three inductor currents have natural time constants $L_j/R_L \approx 20$–40 ms but are driven by the inner-current loops with effective bandwidth $\omega_{inner} = 1000$ rad/s (time constant 1 ms), one order of magnitude faster than the outer-voltage loop bandwidth ($\omega_{outer} = 100$ rad/s). Assuming the inner loops have reached their quasi-stationary references i_{pv}^*, i_{bat}^*, i_{el}^*, the slow manifold dynamics on V_{bus} become [49]

$$C_{bus}\, \frac{dV_{bus}}{dt} = (1 - u_{pv})\, i_{pv}^* + u_{bat}\, i_{bat}^* - u_{el}\, i_{el}^* \tag{23}$$

Substituting the quasi-stationary duty cycle expressions $u_{bat,ss} = V_{bat}/V_{bus}$, $u_{el,ss} = V_{el}/V_{bus}$, $(1 - u_{pv,ss}) = V_{pv}/V_{bus}$ (obtained by zeroing the inductor voltage equations in (8)), this reduces to a power-balance equation that highlights the role of the battery current i_{bat}^* as the actuator for V_{bus} regulation. The IDA-PBC design then provides i_{bat}^* as a function of the bus-voltage error.

Defining the bus-voltage tracking error $\tilde{V}_{bus} = V_{bus} - V_{bus}^*$ and an integral state ξ with $\dot{\xi} = \tilde{V}_{bus}$, the desired closed-loop Hamiltonian on the reduced state $\mathbf{x}_c = [\tilde{V}_{bus},\, \xi]^T$ is chosen as the quadratic form

$$H_d(\mathbf{x}_c) = \frac{1}{2}\, C_{bus}\, \tilde{V}_{bus}^2 + \frac{1}{2}\, K_i\, \xi^2 \tag{24}$$

with the desired closed-loop matrices

$$J_d = \begin{bmatrix} 0 & -1 \\ 1 & 0 \end{bmatrix}, \qquad R_d = \begin{bmatrix} G_d & 0 \\ 0 & 0 \end{bmatrix} \tag{25}$$

where $G_d > 0$ is the damping injection gain (with units of conductance, A/V) and $K_i > 0$ is the integral gain. The non-trivial J_d introduces a skew-symmetric coupling between the voltage error and the integral state, contrasting with the 1×1 reduction of [37], where J_d was absent. Matching the closed-loop dynamics yields the IDA-PBC control law for the battery-current reference:

$$i_{bat}^{*} = \frac{V_{bus}}{V_{bat}} \left[-(1 - u_{pv})\, i_{pv} + u_{el}\, i_{el} - G_d\, \tilde{V}_{bus} - K_i\, \xi \right] \tag{26}$$

which is then tracked by the inner battery-current loop via damping injection:

$$u_{bat} = \frac{V_{bat} - R_L\, i_{bat} - R_{d,bat}\, (i_{bat}^{*} - i_{bat})}{V_{bus}} \tag{27}$$

where $R_{d,bat} = L_{bat}\, \omega_{inner} = 1\ \Omega$ is the virtual damping resistance chosen to enforce the inner-loop bandwidth. Analogous expressions are obtained for the PV and electrolyzer inner-current loops. Stability of the closed loop is established by (19)

$$\dot{H}_d = -G_d\, \tilde{V}_{bus}^{2} \leq 0 \tag{28}$$

with asymptotic convergence to $\tilde{V}_{bus} = 0$, $\xi = \xi^{*}$ guaranteed by LaSalle's principle whenever $G_d > 0$ and the inner-current loops are stable. This certificate holds for the reduced two-state system on the slow manifold, under the assumptions that (i) the inner-current loops track their references with a time constant at least one order of magnitude shorter than the outer loop, (ii) the plant model used in (26) matches the physical plant, (iii) the battery-current reference is not saturated, and (iv) $V_{bat} > 0$ and $V_{bus} > 0$. It is therefore a stability result for the slow dynamics of the nominal closed loop, not a global proof for the complete seven-state system under saturation, model mismatch and time-varying disturbances. Robustness to those conditions is assessed numerically in Sections 3.3 and 3.4; a Lyapunov analysis of the full system with the anti-windup logic active is left for future work.

The damping gain G_d and integral gain K_i are not selected heuristically. The closed-loop linearization around the equilibrium of (25) yields the characteristic polynomial

$$s^{2} + \frac{G_d}{C_{bus}}\, s + \frac{K_i}{C_{bus}} = 0 \tag{29}$$

Matching this to the prescribed outer-loop specification $\omega_n = \omega_{outer}$ uniquely determines the gains as a function of the desired damping ratio. In the present implementation, G_d is selected such that the closed-loop crossover matches the PI cascade crossover frequency, giving $G_d = C_{bus}\, \omega_{outer} = 0.220$ A/V, while K_i is selected slightly above the pure second-order matching value to favor a faster rejection of bus-voltage offsets caused by parametric uncertainty in V_{bat}, yielding $K_i = 25$ A/(V·s). This choice corresponds to $\omega_n \approx 107$ rad/s and $\zeta \approx 0.47$ on the linearized response, which is slightly underdamped but ensures a faster integral correction without compromising stability. This analytical tuning procedure ensures all three controllers operate with comparable bandwidth, providing a fair basis for comparison and avoiding heuristic selection of the damping parameter. The deviation from the nominal damping target ($\zeta \approx 0.47$ instead of 0.707) is thus confined to the outer loop and disclosed explicitly, while the crossover frequency remains matched to the PI and IO-FL designs; the comparison is therefore performed at matched bandwidth rather than at strictly identical damping. Because damping affects overshoot and integral-error metrics, a retuned variant with $G_d = 2\zeta\omega_{outer}C_{bus} = 0.311$ A/V and $K_i = C_{bus}\omega_{outer}^{2} = 22$ A/(V·s), which places the outer loop exactly at $\omega_n = 100$ rad/s and

$\zeta = 0.707$, is included in the ablation study of Section 2.6.4 to verify that the ranking does not depend on this choice.

Relation to IO-FL

Substituting the quasi-stationary duty cycles into (26) and comparing with (16) shows that the two bus-voltage laws share the same structure: the same power-balance feed-forward $(V_{bus}/V_{bat})[-(1-u_{pv})i_{pv} + u_{el}i_{el}]$ and a proportional term whose gains coincide when $G_d = C_{bus}\, k_{V_{bus}}$, which is the case for the matched-bandwidth tuning adopted here (G_d = 0.220 A/V, $C_{bus}k_{V_{bus}}$ = 0.220 A/V). The inner-current loops coincide as well, since the damping injection $R_{d,j} = L_j\omega_{inner}$ reproduces the pole placement L_jk_j of the feedback-linearized loops, and the PV loops are identical. The only term that distinguishes the two laws is the integral action $K_i\xi$ with its anti-windup. On this plant, therefore, IDA-PBC is IO-FL with an integrator on the bus-voltage error, obtained through a different design route: feedback linearization arrives at the law by exact cancellation, IDA-PBC arrives at it by matching the closed loop to a target port-Hamiltonian structure, which in exchange yields the energy-based stability certificate above and a physical reading of the gains (G_d as a virtual conductance, R_d as a virtual resistance). The coincidence is not an implementation artifact but a property of the problem: for a bus capacitor driven by a current actuator through fast inner loops, the matching equation has a unique solution of the assumed quadratic form, and that solution is the cancellation law plus integral action. Section 3.2 confirms the equivalence numerically.

2.6.4. Ablation Variants

Two questions cannot be answered with the three controllers alone: whether the regulation benefit of the nonlinear designs comes from their structure or from the model-based feed-forward they embed, and whether the IAE penalty of IO-FL is intrinsic to feedback linearization or only to its canonical form without integral action. Three variants are therefore added to the comparison, each changing a single element of a baseline controller:

- PI+FF: the PI cascade of Section 2.6.1 with the power-balance feed-forward of (16) added to the battery-current reference,

$$i^*_{bat} = \frac{V_{bus}}{V_{bat}}\Big[-(1-u_{pv})\,i_{pv} + u_{el}\,i_{el}\Big] + K_p^{out}\,\tilde{V}_{bus} + K_i^{out}\int \tilde{V}_{bus}\,dt \tag{30}$$

  where V_{bat} is obtained from the battery model (in practice, from the measured terminal voltage). The outer PI acts on the residual of the power balance; all gains, inner loops, and anti-windup logic are those of the PI cascade.
- IO-FL+I: the canonical IO-FL of Section 2.6.2 with an integral term $-K_i\xi$, $\dot{\xi} = \tilde{V}_{bus}$, inside the bracket of (16), with the same gain K_i = 25 A/(V·s) and back-calculation anti-windup as IDA-PBC. By the argument of Section 2.6.3, this variant is expected to reproduce IDA-PBC exactly.
- IO-FL+I (ζ = 0.707): the same variant with $k_{V_{bus}} = 2\zeta\omega_{outer}$ = 141 rad/s and K_i = 22 A/(V·s), i.e., the retuned IDA-PBC gains of Section 2.6.3.

All six controllers are evaluated under identical scenarios, solver settings, and metric windows, and the degradation and economic post-processors are applied to all of them.

2.7. Component Degradation Models

Two post-processor aging models are integrated into the simulation pipeline. Both operate on the simulated current, voltage, and temperature trajectories of the battery and electrolyzer, producing the first-year capacity loss (battery) and the voltage degradation rate

(electrolyzer) for each control strategy and scenario. Every stress factor that enters the two models (mean state of charge, depth of discharge, RMS currents, mean temperatures, hours of operation) is evaluated as a time-weighted integral of the trajectory, so that the results do not depend on the distribution of the output points of the variable-step solver, which differs between controllers. The two models were developed and validated experimentally by their authors on specific cells and stacks under laboratory protocols; what is validated is the functional form and the parameter values for those devices, not their application to the present pack, stack, thermal conditions, and operating profile. They are used here as published, with parameters representative of commercial LFP cells and Nafion-based PEM stacks, and the absolute lifetimes they project should be read as model extrapolations. Two further sources of uncertainty limit the confidence in those absolute figures: the degradation coefficients carry the scatter of the source experiments, which the models do not propagate, and the battery temperature is held at 25 °C in the aging post-processor because the pack thermal dynamics are not modeled, whereas calendar aging is strongly temperature dependent. The comparison across controllers, which is the object of this work, relies only on the models being applied identically to all of them.

2.7.1. LFP Battery Aging

The battery aging model follows Naumann et al. [14,15], who developed and experimentally validated calendar and cycle aging laws for commercial LFP/graphite cells. The total capacity loss per year is decomposed as

$$\Delta C_{loss}\,[\%/\mathrm{yr}] = \Delta C_{cal} + \Delta C_{cyc} \tag{31}$$

The calendar component depends on the average state of charge $\overline{SOC}$ and an Arrhenius-corrected temperature factor:

$$\Delta C_{cal} = k_{cal,ref}\,\exp\left[-\frac{E_a}{R_g}\left(\frac{1}{\overline{T}_{bat}} - \frac{1}{T_{ref}}\right)\right] f(\overline{SOC})\,\sqrt{t_{yr}} \tag{32}$$

with $k_{cal,ref}$ = 0.11%/$\sqrt{\mathrm{day}}$ at T_{ref} = 25 °C and $\overline{SOC}$ = 0.5, activation energy E_a = 24,500 J/mol, and the SOC factor $f(\overline{SOC}) = 0.45 + 1.10\,\overline{SOC}$. The cycle component depends on the equivalent full cycles per year (EFC) and the mean depth of discharge:

$$\Delta C_{cyc} = (a + b\,\overline{DOD})\,\sqrt{EFC_{yr}} \tag{33}$$

with a = 0.015%/$\sqrt{\mathrm{EFC}}$ and b = 0.05%/$\sqrt{\mathrm{EFC}}$. EFC is computed from the simulated current trajectory as

$$EFC_{yr} = \frac{1}{2\,Q_{nom}}\int_0^{t_{sim}} |i_{bat}(t)|\,dt \cdot \frac{8766}{t_{sim,h}} \tag{34}$$

The factor $8766/t_{sim,h}$ in Equation (34) extrapolates the observed throughput to an annual basis under continuous operation and is retained in Sections 3.2 and 3.6 for comparability with the stress scenario. For the economic analysis (Section 2.8.4), the cycle term is annualized instead with the operating hours of the techno-economic model, h_{op} = 2400 h/yr, so that the physical and economic calculations share one operating schedule; the calendar term always accrues over the full year. Because the Naumann laws are proportional to $\sqrt{t}$ and $\sqrt{EFC}$, the quantity reported as "capacity loss per year" is the loss accumulated during the first year, not a constant annual rate: the loss after t years is $\Delta C_{loss}(1\,\mathrm{yr})\sqrt{t}$, and the time to the 80% end-of-life criterion follows from that expression. The representative day

of Section 3.5 provides, in addition, a direct estimate of the throughput under supervisory operation that does not rely on extrapolating the stress window.

The end-of-life criterion is taken as 80% of nominal capacity, consistent with [15].

2.7.2. PEM Electrolyzer Degradation

The PEM degradation model follows Frensch et al. [10], who quantified the voltage degradation rate as the sum of a baseline term and three accelerating contributions related to current ripple, ON/OFF cycling, and excess temperature:

$$\left.\frac{dV_{el}}{dt}\right|_{aging} = U_{base} + k_j\, j_{ripple,RMS} + k_{cyc}\, n_{cycles/h} + k_T\, \max(0, \overline{T}_{el} - T_{ref}) \tag{35}$$

with U_{base} = 5 µV/h baseline rate under steady operation, k_j = 80 µV/h per A/cm^2 ripple sensitivity, k_{cyc} = 2 µV/h per cycle/h from start/stop contribution [11], k_T = 2 µV/h per K excess above T_{ref} = 60 °C, and $j_{ripple,RMS}$ computed as the time-weighted standard deviation of the current density during operation (excluding standby periods). The cycling frequency $n_{cycles/h}$ is the number of start/stop cycles divided by the hours of stack operation (current above 1 A) in the simulated window, which is the same time basis on which the rate is expressed and later annualized. The end-of-life criterion is taken as a 10% increase in stack voltage above the initial value at nominal current, consistent with the standard +10% criterion [11] and recent durability reviews [8]. The rate is expressed per hour of operation. In Sections 3.2 and 3.6, it is annualized under continuous operation (8766 h/yr); in the economic analysis, it is annualized with the 2400 h/yr operating schedule of the techno-economic model. Expressed in operating hours, the +10% criterion is reached after approximately 2.3×10^5 h, which exceeds the industrial stack lifetime specification quoted below and confirms that the projection is not binding. It is applied at the stack level against this criterion, and the corresponding projection is used as an effective end-of-life indicator for the cross-controller comparison rather than as an absolute lifetime prediction; absolute replacement timing in the economic analysis is governed instead by the calendar cap of Section 2.8.4, consistent with industrial stack lifetime specifications of 40,000–80,000 h. The ON/OFF cycling frequency $n_{cycles/h}$ is computed from threshold crossings (1 A) of the simulated current rather than assumed; it is zero in the stress scenario, where the set-point is constant, and non-zero in the representative day of Section 3.5, where the supervisory layer starts and stops the stack. In that scenario, the ripple term is evaluated on the tracking error $i_{el} - i_{el}^*$ rather than on the deviation from the window mean, since the set-point itself varies with the irradiance. Both aging models are applied identically to the trajectories generated by the six controllers, ensuring a like-for-like comparison.

2.8. Simulation Scenarios and Performance Metrics

2.8.1. Operating Scenarios

The deterministic evaluation uses a stress profile superimposing six abrupt cloud drop-out events of 5–20 s duration, with irradiance dropping to 150–400 W/m^2—a standard benchmark disturbance for PV-coupled hydrogen systems [7]. The electrolyzer set-point is held at 30 A by the supervisory layer and the PV reference at V_{pv}^* = 249 V, so this scenario isolates the converter-level response to irradiance disturbances.

Representative Day with Supervisory Operation

To represent the operating conditions that the stress scenario excludes (daily irradiance variation, low-generation periods, electrolyzer start/stop, and state-of-charge limits), a second scenario simulates the daylight hours of a representative day in the Atacama Desert, from 05:30 to 20:30, with a synthetic irradiance model (clear-sky envelope for latitude

24° S at the equinox, G_{peak} = 1050 W/m^2, multiplied by an Ornstein–Uhlenbeck cloud index). Two days are considered: a clear day (cloud-index mean 0.88) and a cloudy day (mean 0.75 and a larger diffusion coefficient), on which three deep cloud passages lasting 8–15 min are superimposed at 10:30, 13:15, and 15:40 to force deliberate start/stop events. A supervisory layer common to all controllers provides the references. An ideal maximum-power-point tracker computes $V^*_{pv}(G, T)$ from the single-diode model. The electrolyzer set-point follows the available PV power, $i^*_{el} = \eta_c P_{mpp}(G)/V_{el,nom}$ with η_c = 0.95, bounded to $[I_{min}, I_{nom}] = [4, 40]$ A and rate-limited to 2 A/s. The stack is started when $G > 200$ W/m^2 for 120 s and stopped when $G < 100$ W/m^2 for 120 s; the PV converter is enabled when $G > 80$ W/m^2 and disabled below 30 W/m^2 with a 60 s dwell. The set-point is driven to zero if the battery state of charge falls below 20%, and the PV current is curtailed above 95%. Because the supervisory decisions are computed from the irradiance profile, the start/stop schedule is identical for all controllers by construction, which is what a converter-level comparison requires; the state-of-charge limits act in closed loop and could differ between controllers but are not reached on either day. The lumped thermal model of the stack dissipates only to ambient through R_{th} and would exceed 130 °C in sustained operation; a proportional cooling loop (150 W/K above 60 °C), representing the thermal management of the balance of plant, holds the stack near its operating temperature. This loop is irrelevant over the 10 min stress window and is used only in the daily scenario. Three implementation details of the PI cascade, exercised only by start/stop operation, were corrected for this scenario. The duty-cycle feed-forward of the electrolyzer loop is anchored at the zero-current duty $V_{rev}N_{cells}/V_{bus}$ and rises linearly to its original value at 30 A; the original feed-forward, proportional to the set-point, drove the duty cycle to zero in standby, and a reverse current then circulated through the idle stack, which the averaged model does not prevent. The standby limit on that duty cycle, which left a residual negative voltage across the inductor resistance, was set to the zero-current equilibrium. An undefined gain name in the anti-windup branch of the battery-current loop, reached only when the battery duty cycle saturates, was corrected. The integrators of the PV and electrolyzer loops are reset at each start, which is standard practice for a bumpless restart. None of these changes affects the stress or Monte Carlo results, where the set-point is constant at 30 A, the feed-forward takes its original value, and the duty cycle does not saturate; re-running the stress scenario with the corrected PI reproduces the results of Section 3.2 exactly.

All scenarios use the MATLAB `ode23tb` stiff solver (relative tolerance 10^{-4} and absolute tolerance 10^{-6} for the deterministic stress runs, 5×10^{-3} and 10^{-4} for the 2400 Monte Carlo runs, and 10^{-3} and 10^{-5} for the representative-day scenario, with integration split at the switching instants of the supervisory layer) with fixed random seeds for reproducibility.

2.8.2. Performance Metrics

The analysis adopts a comprehensive set of metrics computed from the steady-state portion of each simulation (after discarding the first 5% of the trajectory as transient):

- The standard deviation σ and peak-to-peak excursion of V_{bus};
- The maximum absolute deviation of V_{bus} from the reference, expressed in V and as a percentage;
- The integral of absolute error (IAE) and the integral of time-weighted absolute error (ITAE) of V_{bus};
- The root-mean-square ripple of the electrolyzer current i_{el};
- The root-mean-square value of the battery current i_{bat}.

2.8.3. Statistical Analysis

A Monte Carlo experiment of $N = 200$ paired runs is performed on the stress scenario: converter series resistances are perturbed by ±30%, inductances and capacitances by ±20%, and the battery EMF E_0 and the electrolyzer ohmic resistance by ±5%, sampled from independent uniform distributions with fixed seeds. The same perturbation set is applied to the six controllers within each run, enabling paired two-tailed Student's t-tests ($df = 199$) with 95% confidence intervals. In this set, the controllers use the perturbed parameter values, so it quantifies sensitivity to plant variation with the controller retuned to each plant. A second set of $N = 200$ paired runs addresses robustness to model error. The plant is perturbed as above, but the controllers operate with the nominal parameters, and the quantities that the model-based laws invert are corrupted inside the controller: the PV short-circuit current (±5%), the stack ohmic resistance (±10%) and anodic exchange current density (one half-decade), and the battery EMF (±3%) and internal resistance (±20%). The measurements are corrupted as well: irradiance (±10%); ambient temperature (±5 K); bus voltage (a bias of ±1 V plus a low-frequency error of 0.5 V RMS in the 0.05–5 Hz band, representing drift and residual noise after the anti-aliasing filter); and the gains of the three current sensors (±2%). All controllers see the same corrupted measurements within a realization. The ±2% bus-voltage band used as the compliance criterion in both sets is a design target adopted in this work, chosen so that bus excursions remain small compared with the input-voltage margin of the electrolyzer converter; it is not prescribed by an external standard, and Section 3.3 reports the compliance fraction over a range of thresholds so that readers with a different target can read the result for it.

2.8.4. Economic Analysis Methodology

A net present value (NPV) model is implemented to compute the levelized cost of hydrogen (LCOH) for each controller, defined as the ratio of the present value of total system costs to the present value of hydrogen production over the project horizon:

$$\mathrm{LCOH} = \frac{\mathrm{CAPEX} + \mathrm{NPV}(\mathrm{OPEX}) + \mathrm{NPV}(\mathrm{Replacements})}{\mathrm{NPV}(m_{H_2})} \tag{36}$$

where each annual cash flow is discounted at the weighted average cost of capital (WACC) over a T-year horizon. The total capital expenditure (CAPEX) is decomposed into PV array, battery, PEM electrolyzer, DC–DC converters, balance of plant (15% of subsystem CAPEX), and installation (10% of CAPEX plus balance of plant). The operating expenditure (OPEX) includes annual O&M (2.5% of CAPEX), deionized water consumption, and fixed annual costs. Replacement cash flows are triggered by the degradation rates obtained from the Naumann (battery) and Frensch (PEM) models of Sections 2.7.1 and 2.7.2, applied to the corresponding end-of-life criteria: 80% remaining capacity for the battery [15] and the lesser of (i) +10% stack voltage [11] or (ii) a maximum calendar lifetime of 10 years [51] for the PEM. Hydrogen production is computed from the Faraday law applied to the simulated electrolyzer current of each controller, with the Faraday efficiency η_F of Equation (6) evaluated at the instantaneous current density, so that any controller-dependent difference in current tracking enters the LCOH; the production rate is referred to the 2400 h/yr operating schedule. Replacement cash flows follow a convention that is consistent with the project horizon: a component is replaced when its end of life falls strictly inside the horizon, and the unused fraction of the life of a replaced component at the end of the horizon is credited as a linear residual value. The alternative convention, which charges a replacement falling exactly at the end of the horizon in full and credits no residual value, is retained as a sensitivity case. The battery cycle term and the PEM degradation rate are annualized with the same 2400 h/yr used for production (Section 2.7).

All economic parameters and sources are summarized in Table 2; values correspond to small-scale off-grid installations (4–10 kW), which exhibit higher unit costs than utility-scale benchmarks. A 10-year calendar replacement cap is adopted for both the battery and the PEM stack. For the battery, it corresponds to the ten-year product and performance warranty offered for stationary LFP packs in the 5–25 kWh class [52]; for the PEM stack, it corresponds to the lower end of the 50,000–80,000 h stack lifetimes reported for current technology [51], which, at 2400 h/yr, span 21–33 years, truncated to the warranty horizon that governs replacement decisions in remote installations. The aging models project longer lives than this cap under the present operating profile (Section 3.6), so the replacement schedule is controller-independent by construction: no controller reaches an aging-based end of life inside the horizon. This is stated explicitly because it bounds what the LCOH comparison can show. To make the result independent of the cap, a variant in which replacement is governed solely by the aging models, with no calendar limit, is reported alongside the base case. This cap pertains to managed stationary LFP storage operated within controlled state-of-charge and thermal windows and should not be conflated with automotive SLI or NMC batteries, whose 3–5-year field lives reflect harsher duty cycles, wider temperature excursions, and a different cell chemistry. To assess robustness, sensitivity scenarios are evaluated on CAPEX (±30%), WACC (5% and 10%), project horizon (15 and 20 years), operating hours (3500 h/yr, Atacama with single-axis tracking), the replacement convention, the calendar cap, and the battery size (5–20 kWh), reported in Section 3.7.

Table 2. Economic parameters used in the LCOH analysis. All values correspond to small-scale off-grid installations in northern Chile; 2024 baseline.

Parameter	Symbol	Value	Source
Financing and horizon			
Weighted avg. cost of capital	r	7%	[2]
Project horizon	T	10 years	[2]
Unit costs (small-scale 2024 baseline)			
PV array	c_{PV}	1200 USD/kWp	[4]
Battery LFP system level	c_{bat}	400 USD/kWh	[20]
PEM electrolyzer installed	c_{PEM}	1500 USD/kW	[19]
DC–DC converters	c_{conv}	150 USD/kW	engineering estimate
Balance of plant (frac. of components)	f_{BoP}	15%	[20]
Installation (frac. of CAPEX+BoP)	f_{inst}	10%	[20]
Operating expenditure			
O&M (frac. of CAPEX/yr)	$f_{O\&M}$	2.5%	[19]
Deionized water cost	c_{H_2O}	0.05 USD/kg H_2	engineering estimate
Fixed annual OPEX	$C_{f,yr}$	200 USD/yr	engineering estimate
Replacement criteria			
Battery EOL (remaining capacity)	–	80%	[15]
PEM EOL (voltage increase)	–	+10%	[11]
PEM maximum calendar lifetime	–	10 years	[51]
Battery maximum calendar lifetime	–	10 years	[52]
Battery replacement cost factor	$f_{rep,bat}$	1.0× CAPEX	full system
PEM replacement cost factor	$f_{rep,PEM}$	0.6× CAPEX	[19]
Operation			
Annual operating hours	h_{op}	2400 h/yr	[3]
Electrolyzer operating current	i_{el}^{*}	30 A (simulated i_{el})	system rating

Applying the unit costs of Table 2 to the system sizing of Table 1 yields a total CAPEX of 22,335 USD, decomposed as 5760 USD for the PV array, 4096 USD for the battery, 6000 USD for the PEM stack, 1800 USD for the three DC–DC converters (rated 4 kW each), 2648 USD for balance of plant, and 2030 USD for installation.

3. Simulations and Results

The three control strategies and the three ablation variants are evaluated through five complementary analyses: deterministic transient performance, statistical robustness to plant variation, robustness to model mismatch and measurement error, a representative day with supervisory start/stop operation, and long-term component degradation. All simulations use the averaged converter model in MATLAB with $V_{bus}^{\star}$ = 400 V. The deterministic scenario consists of repeated cloud drop-out events (G: 900 $\rightarrow$ 250 W/m^2) over a 10 min window, with the electrolyzer current set-point held constant at i_{el}^{*} = 30 A by the supervisory layer. The first statistical analysis comprises $N = 200$ Monte Carlo realizations with electrical parameters perturbed by $\pm$20–30% and electrochemical parameters by $\pm$5%; the second repeats it with the controllers operating on nominal models and corrupted measurements. Component aging is computed with the Naumann LFP model [14,15] and the Frensch PEM model [10]. The first 5% of each window is discarded from the metrics as an initial transient.

3.1. Deterministic Stress Test

Figure 5 shows the response to a representative cloud drop-out at t = 60 s (G: 900 $\rightarrow$ 250 W/m^2). The PI controller exhibits a V_{bus} dip of 16 V (4.0%; the deepest of the six events, at t = 240 s with $G \rightarrow$ 150 W/m^2, reaches the 18.3 V reported in Table 3), returning to within 1 V of the reference after 40 ms with a visible overshoot of about 1 V, whereas IO-FL and IDA-PBC limit the excursion to 3.2 V (0.8%) and PI+FF to 2.2 V (0.55%). During the transient, IO-FL and IDA-PBC restore maximum-power-point tracking within tens of milliseconds, against a noticeably slower re-convergence for PI. The battery current steps from -7 A (charging) to $\approx$+9 A (discharging): PI overshoots to $\sim$12 A and settles slowly, IO-FL and IDA-PBC peak at $\sim$11 A and settle within 50 ms, and the feed-forward of PI+FF commands a brief spike of $\sim$16 A at the instant of the drop-out, which is what buys its smaller dip. The electrolyzer current i_{el} is unaffected for IO-FL and IDA-PBC and deviates by 0.2 A peak-to-peak for PI+FF and by 0.4 A for PI.

3.2. Quantitative Performance Metrics

Figure 6 summarizes four key indicators over the full 600 s stress window, and Table 3 provides the complete metric set for the six controllers. Three observations organize the results.

First, the integrator-augmented IO-FL and IDA-PBC are the same controller. Their trajectories differ by at most 1.5 mV in V_{bus} and 3 mA in i_{bat} over the whole window, which is the solver tolerance, and every metric coincides to three significant figures (0.884% peak deviation, 0.588 V·s IAE). This is the numerical counterpart of the structural argument of Section 2.6.3.

Second, the peak-suppression benefit comes from the power-balance feed-forward, not from the nonlinear structure. The canonical IO-FL already reduces the peak deviation from 4.57% to 0.91% with no integral action at all; adding the same feed-forward term to the PI cascade (PI+FF) reduces it further, to 0.65%, with a peak-to-peak excursion of 4.9 V against 5.9 V for IO-FL and IDA-PBC. The PI+FF variant keeps the five PI integrators, so it also has the lowest IAE of the set (0.092 V·s, six times lower than IDA-PBC) and the lowest ITAE. The ordering PI+FF < IDA-PBC holds for every bus-voltage metric.

Third, the IAE ordering of the original three controllers (IO-FL > PI > IDA-PBC) is entirely a matter of integral action: IO-FL yields 15.82 V·s because a residual offset of tens of millivolts accumulates over the window, and the same law with the $K_i\xi$ term yields 0.59 V·s. Retuning the outer loop to ζ = 0.707 (IO-FL+I, ζ = 0.707) improves IDA-PBC moderately (0.84% peak, 0.41 V·s IAE) and does not change its position relative to PI+FF,

so the ranking reported here is not a consequence of the damping difference disclosed in Section 2.6.3.

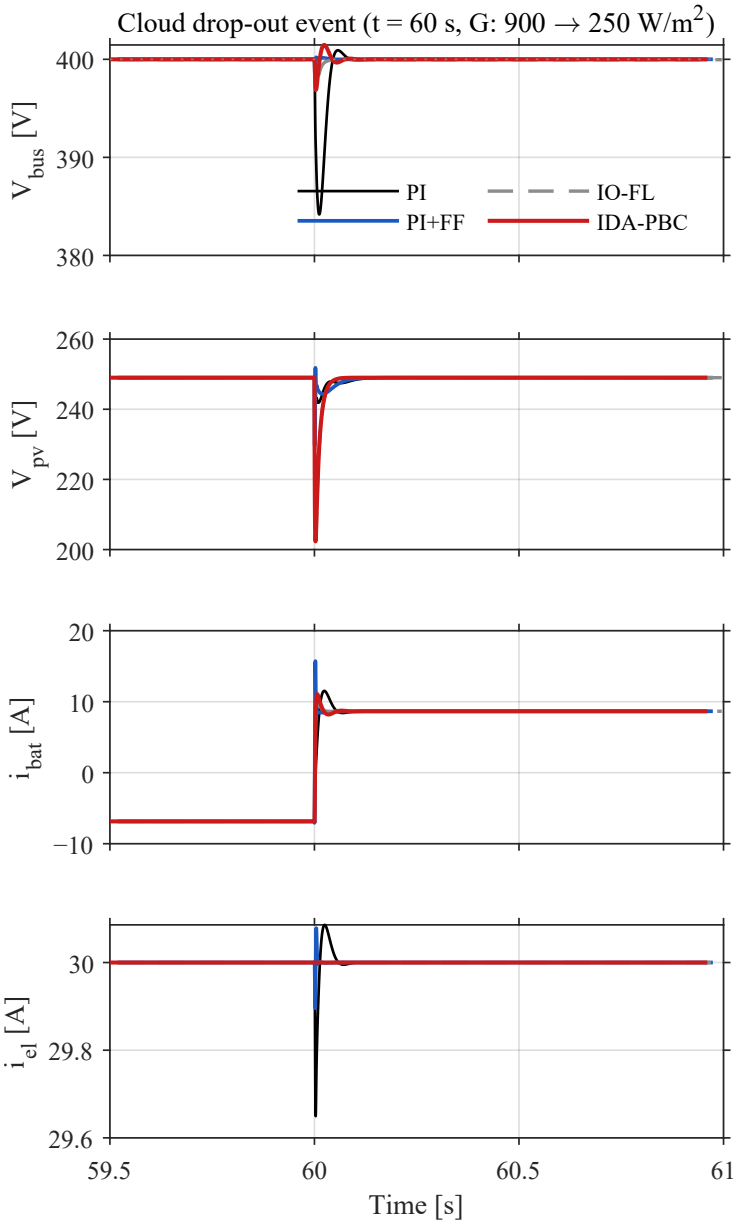


Figure 5. Time-domain response of the PI cascade, PI+FF, IO-FL, and IDA-PBC to a cloud drop-out event at t = 60 s (G: 900 → 250 W/m^2). The IDA-PBC controller maintains V_{bus} within ±5 V and isolates the electrolyzer current from the disturbance; PI+FF limits the dip further at the cost of a brief battery-current spike; at this scale, the IO-FL trace is nearly indistinguishable from the IDA-PBC trace.

The electrolyzer current ripple at the control-loop bandwidth is suppressed to numerical zero by the four model-based variants, against 0.003 A RMS for PI and 0.0007 A for PI+FF, whose PI electrolyzer loop still sees a small bus disturbance. This metric captures only controller-induced ripple within the loop bandwidth; the PWM switching ripple at f_{sw} = 20 kHz (typically 1–3% of rated current) is not represented by the averaged model. We assume it to be common to all implementations because it is set by the converter design (topology, inductor, switching frequency, and operating point) rather than by the outer control law; interleaved topologies, for instance, reduce it substantially in simulation and experimentally [53,54] without any change in the outer loop. This is an expectation to be confirmed with a switched model or experimentally for this plant, not a result of this study.

The values close to zero therefore indicate near-perfect tracking within the averaged model and should not be read as physical ripple levels (Section 3.6).

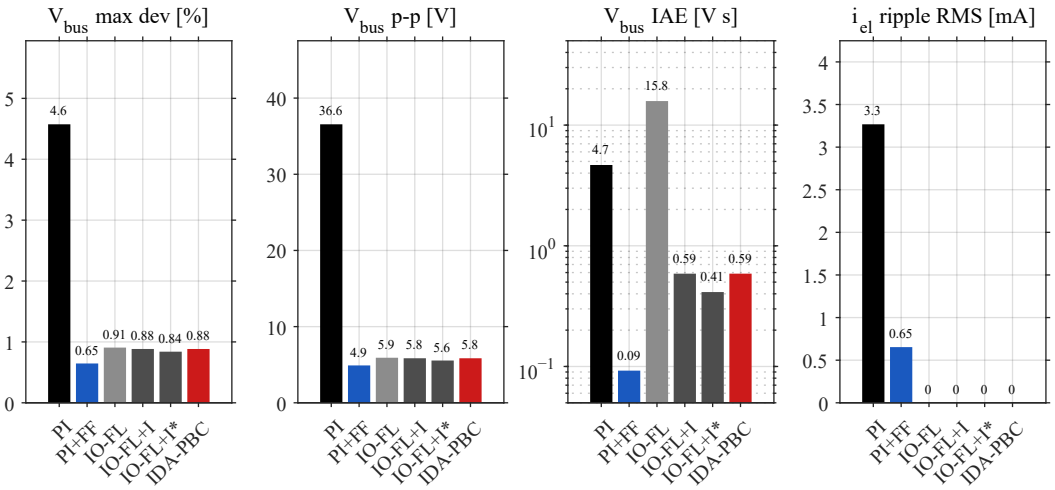


Figure 6. Performance metrics over the 600 s stress scenario for the six controllers. The power-balance feed-forward (PI+FF, IO-FL, IO-FL+I, IDA-PBC) sets the peak metrics; integral action sets the accumulated-error metrics; IO-FL+I and IDA-PBC coincide. IO-FL+I*: IO-FL+I retuned to $\zeta = 0.707$.

Table 3. Performance metrics over the deterministic stress scenario (600 s, $V^{\star}_{bus}$ = 400 V, first 5% of the window excluded as an initial transient). PEM degradation and projected lifetimes use the continuous-operation annualization (8766 h/yr) for comparability with Section 3.6; the operating-hour basis is used in Section 3.7.

Metric	PI	PI+FF	IO-FL	IO-FL+I	IO-FL+I ζ = 0.707	IDA-PBC	Units
Bus-voltage regulation							
V_{bus} std	2.926	0.329	0.453	0.435	0.399	0.435	V
V_{bus} peak-to-peak	36.56	4.91	5.91	5.85	5.55	5.85	V
V_{bus} max deviation	18.30	2.58	3.63	3.54	3.36	3.54	V
V_{bus} max deviation	4.57	0.65	0.91	0.88	0.84	0.88	%
V_{bus} IAE	4.67	0.092	15.82	0.588	0.414	0.588	V·s
V_{bus} ITAE	1366	27	4970	171	121	171	V·s^2
Component stress indicators							
i_{bat} RMS	6.90	6.90	6.90	6.90	6.90	6.90	A
i_{el} ripple RMS (loop)	0.003	0.0007	$<10^{-12}$	$<10^{-12}$	$<10^{-12}$	$<10^{-12}$	A
Battery degradation (Naumann LFP, 8766 h/yr basis)							
EFC per year	601	601	601	601	601	601	–
First-year capacity loss	2.509	2.509	2.509	2.509	2.509	2.509	%
PEM degradation (Frensch, 8766 h/yr basis)							
dV/dt	42.21	42.21	42.21	42.21	42.21	42.21	µV/h
Efficiency loss	0.385	0.385	0.385	0.385	0.385	0.385	%/yr
Projected years to EOL	25.95	25.95	25.95	25.95	25.95	25.95	years

3.3. Monte Carlo Robustness Analysis

To assess controller sensitivity to plant variation, $N = 200$ Monte Carlo realizations are conducted, each with independently perturbed values of the converter parameters (R_L, L, C, ±20–30%), the battery EMF E_0 (±5%), and the electrolyzer ohmic resistance (±5%). All six controllers are evaluated on identical perturbed plants within each realization to enable paired statistical tests. In this first set, the controllers are given the perturbed parameter values, so that the model-based laws cancel the plant exactly; it therefore measures how the closed loop responds to a different plant when the controller is retuned to it, not robustness to model error. The one exception is IDA-PBC, whose virtual conductance and resistances

are fixed numbers (G_d = 0.220 A/V, $R_{d,j} = L_{j,nom}\omega_{inner}$) and are not updated with the perturbed L and C; this is why its dispersion is slightly larger than that of IO-FL+I below, although the two laws coincide for the nominal plant. Robustness to model mismatch proper is the object of Section 3.4. The seed of the random number generator is fixed by the realization index, ensuring full reproducibility of the experiment. Figure 7 shows box plots of four representative metrics, and Figure 8 presents the empirical cumulative distribution functions (ECDFs) of the maximum V_{bus} deviation and the IAE.

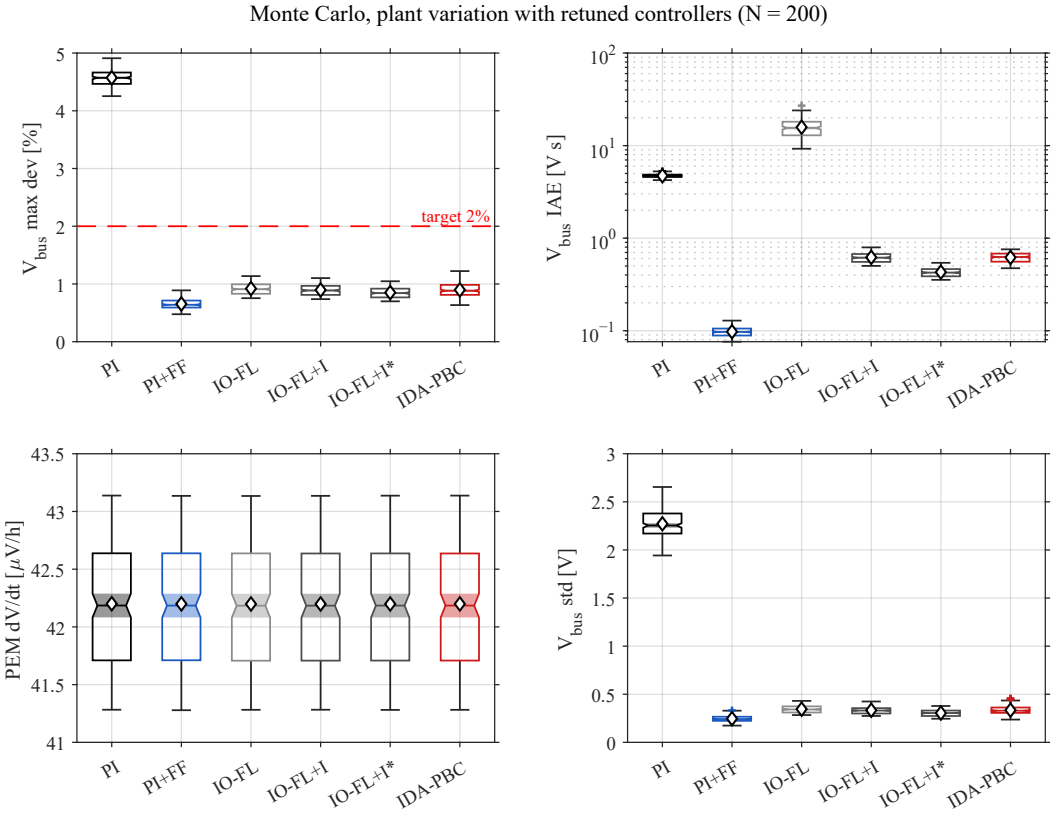


Figure 7. Monte Carlo distributions ($N = 200$) of four key metrics for the six controllers. Notched box plots indicate 95% confidence intervals on the medians; white diamonds mark the means. The four variants with the power-balance feed-forward share the same peak-suppression band, PI+FF sits below it, and integral action separates the IAE distributions. The PEM voltage degradation rate differs by less than 0.1 µV/h across the six controllers. IO-FL+I*: IO-FL+I retuned to $\zeta = 0.707$.

The statistical results (Table 4) confirm the deterministic findings. Regulation compliance is the most consequential outcome: 100% of the realizations of the five variants that carry the power-balance feed-forward satisfy the ±2% target on V_{bus} (worst cases between 0.89% for PI+FF and 1.22% for IDA-PBC), whereas 0% of the PI realizations do (best case 4.25%). Paired t-tests yield $p < 10^{-100}$ for all PI-versus-feed-forward comparisons on regulation metrics. PI+FF has a lower peak deviation than IDA-PBC in 200 of 200 realizations (mean difference −0.24 percentage points, $t = -76$) and a lower IAE in 200 of 200 (−0.52 V·s, $t = -112$). IO-FL+I and IDA-PBC are statistically indistinguishable ($p = 0.70$ for the peak deviation, $p = 0.79$ for the IAE), as expected from Section 2.6.3.

The IAE ordering (IO-FL > PI > IO-FL+I = IDA-PBC) is preserved in 100% of realizations, with fully non-overlapping distributions (Figure 8b), establishing that the integrator-related gap between IO-FL and IDA-PBC is a structural property of the formulations rather than a parameter-dependent one.

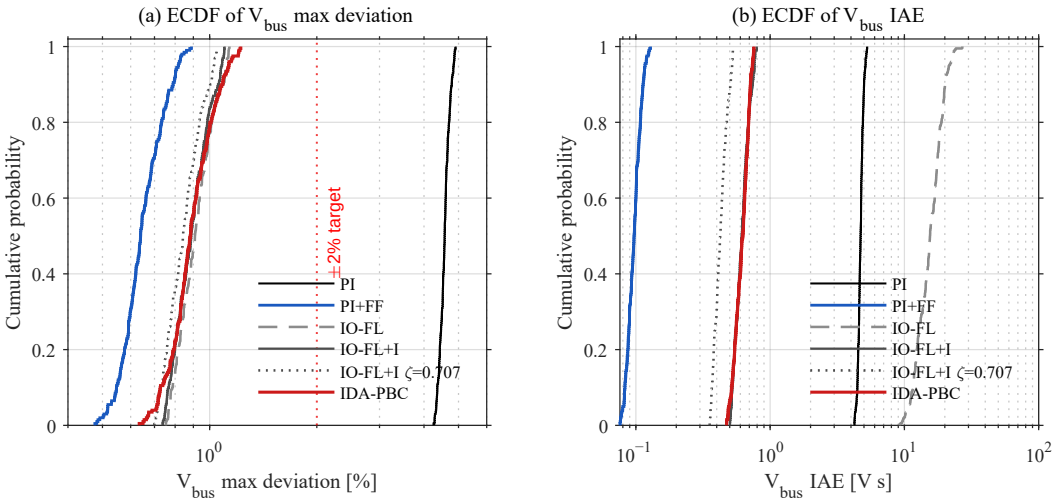


Figure 8. Empirical cumulative distribution functions of (**a**) V_{bus} maximum deviation and (**b**) V_{bus} IAE across $N = 200$ Monte Carlo realizations. The ±2% regulation target is met by 100% of the runs of the five feed-forward variants and 0% of the PI runs. The IO-FL+I trace nearly coincides with the IDA-PBC trace and is hidden beneath it.

Table 4. Monte Carlo statistical summary ($N = 200$ realizations, plant parameters perturbed ±20–30%, controllers retuned to the perturbed plant). All paired t-tests for PI versus the feed-forward variants yield $p < 10^{-100}$ on regulation metrics; IO-FL+I versus IDA-PBC is non-significant on every metric. The PEM dV/dt differs by at most 0.002 µV/h (5×10^{-5} of the rate) between any two controllers. * Retuned to $\zeta = 0.707$.

Metric	PI	PI+FF	IO-FL	IO-FL+I	IO-FL+I *	IDA-PBC
Mean ± std across 200 realizations						
V_{bus} max dev [%]	4.572 ± 0.150	0.654 ± 0.089	0.919 ± 0.105	0.896 ± 0.100	0.851 ± 0.096	0.898 ± 0.128
V_{bus} IAE [V·s]	4.72 ± 0.22	0.098 ± 0.012	15.79 ± 3.42	0.621 ± 0.077	0.430 ± 0.048	0.619 ± 0.074
V_{bus} std [V]	2.271 ± 0.138	0.247 ± 0.033	0.345 ± 0.040	0.334 ± 0.039	0.305 ± 0.035	0.335 ± 0.045
PEM dV/dt [µV/h]	42.20 ± 0.54	42.20 ± 0.54	42.20 ± 0.54	42.20 ± 0.54	42.20 ± 0.54	42.20 ± 0.54
Worst-case V_{bus} max deviation across 200 realizations [%]						
Worst case	4.910	0.889	1.136	1.102	1.047	1.223
Compliance with the ±2% target						
Fraction within target	0%	100%	100%	100%	100%	100%

Because the ±2% figure is an adopted design target rather than a normative limit (Section 2.8), Table 5 reports the compliance fraction over a range of thresholds. The conclusion is insensitive to the threshold between 1.5% and 4%: PI fails, and the five feed-forward variants comply. At 1%, the variants separate (PI+FF 100%, IO-FL+I with $\zeta = 0.707$ 90%, IO-FL+I 84%, IDA-PBC 79%, IO-FL 77%), and at 0.75%, only PI+FF retains a majority of compliant runs.

The Monte Carlo results also reveal a finding of equal importance: the PEM voltage-drift rate is the same for the six controllers, 42.20 ± 0.54 µV/h, despite the complete suppression of electrolyzer ripple by the model-based variants (Table 4). The dispersion of 0.54 µV/h is produced by the plant perturbation, which moves the stack temperature, and is common to all controllers within each realization; the paired differences between controllers are at most 0.002 µV/h (PI against the model-based variants), which is exactly the size of the ripple term of the PI cascade. Because the realizations are paired and $N = 200$, even these differences are formally significant ($p < 0.05$ in twelve of the fifteen pairs), which illustrates that statistical significance carries no physical content here: 0.002 µV/h is

5×10^{-5} of the rate and several orders of magnitude below the uncertainty of the Frensch coefficients. The physical interpretation is developed in Section 3.6.

Table 5. Fraction of Monte Carlo realizations ($N = 200$) whose maximum V_{bus} deviation stays within a given threshold. * Retuned to $\zeta = 0.707$.

Threshold	PI	PI+FF	IO-FL	IO-FL+I	IO-FL+I *	IDA-PBC
±0.75%	0%	83.5%	0%	3.5%	17.5%	12.5%
±1%	0%	100%	76.5%	83.5%	89.5%	78.5%
±1.5%	0%	100%	100%	100%	100%	100%
±2%	0%	100%	100%	100%	100%	100%
±4%	0%	100%	100%	100%	100%	100%
±5%	100%	100%	100%	100%	100%	100%

3.4. Robustness to Model Mismatch and Measurement Error

The second Monte Carlo set (Section 2.8) answers a different question from the first: not how the closed loop responds to a different plant when the controller is retuned to it, but how each controller behaves when its model is wrong and its measurements are corrupted. Table 6 and Figure 9 summarize the $N = 199$ paired realizations.

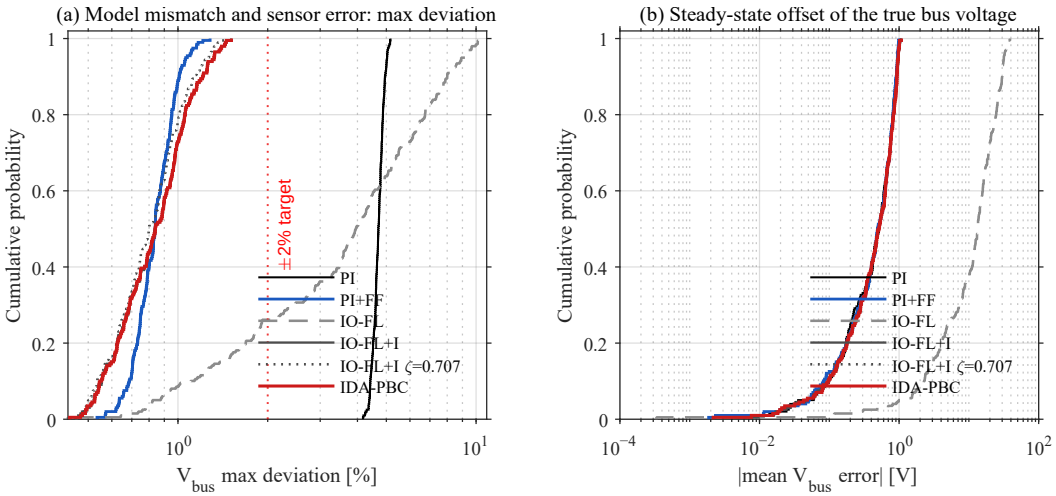


Figure 9. Empirical cumulative distribution functions in the mismatch set of (**a**) the maximum V_{bus} deviation and (**b**) the absolute mean error of the true bus voltage. The canonical IO-FL spreads over an order of magnitude; the four variants with feed-forward and integral action overlap, and the IO-FL+I trace is hidden beneath the IDA-PBC trace.

Three results stand out. First, the canonical IO-FL does not survive model error. Its exact cancellation of the battery voltage and of the converter resistances leaves a steady-state offset proportional to the mismatch, and with the battery-EMF errors considered here (±5% on the plant, ±3% in the controller model) the true bus voltage settles on average 14.4 V away from the reference, up to 38.9 V in the worst realization; its maximum deviation averages 4.29% (worst 10.9%), and only 26% of its realizations meet the ±2% target. The deviation is correlated with the magnitude of the EMF error (correlation 0.57). This is the robustness limitation of the canonical IO-FL that the first Monte Carlo set cannot expose (Section 3.3); it is real, and it is entirely due to the absence of integral action.

Second, the four variants that combine the power-balance feed-forward with integral action keep the target in every realization and converge to the same performance band: mean peak deviations of 0.84, 0.86, 0.83, and 0.86% for PI+FF, IO-FL+I, the retuned variant, and IDA-PBC, with worst cases between 1.28 and 1.51%. The advantage that PI+FF holds

over IDA-PBC when both operate on exact models (0.65 against 0.90% in Table 4) shrinks to 0.017 percentage points here and is no longer significant ($p = 0.24$; PI+FF has the smaller peak in 58% of the realizations). With a wrong model, the exact cancellation of the inner loops is no longer exact for any of them, the feed-forward is computed from corrupted currents and voltages for all of them, and what remains is the same structure, a model-based feed-forward corrected by integral action, which is why they behave alike. IO-FL+I and IDA-PBC remain indistinguishable, as in the first set: their mean peak deviations coincide to three decimals and differ by at most 0.05 percentage points in any single realization. PI remains outside the target in every realization (4.70% mean, 5.16% worst) and exceeds ±5% in 8% of them.

Third, two metrics lose their meaning under measurement error and are reported with that caveat. The mean error of the true bus voltage is about 0.5 V for every controller with integral action because the integrator drives the measured voltage, not the true one, to the reference; the bias of the sensor is reproduced exactly on the bus. The IAE accumulates that bias and the low-frequency measurement error over the window, so it is about 361 V·s for all five variants with integral action and 8185 V·s for IO-FL; it no longer discriminates between controllers and is omitted from the table. The PEM degradation rate again spans less than 0.25 µV/h across the six controllers (41.9–42.1 µV/h), a 0.5% difference below the precision of the Frensch model. Table 7 gives the compliance fraction over thresholds for this set: between 1.5% and 4%, the five feed-forward variants comply, and PI does not; at 1%, PI+FF retains 89% of its realizations against 73–78% for the integral nonlinear variants.

Table 6. Monte Carlo set with model mismatch and measurement error ($N = 199$ paired realizations; controllers with nominal parameters, plant perturbed as in Table 4, model and sensor errors as in Section 2.8; one realization in which the retuned variant failed to integrate is excluded for all controllers). The IAE is omitted because it is dominated by the measurement error for every controller with integral action. * Retuned to $\zeta = 0.707$.

Metric	PI	PI+FF	IO-FL	IO-FL+I	IO-FL+I *	IDA-PBC
V_{bus} max dev, mean ± std [%]	4.700 ± 0.200	0.844 ± 0.133	4.290 ± 2.569	0.861 ± 0.243	0.826 ± 0.225	0.861 ± 0.243
V_{bus} max dev, 95th percentile [%]	5.029	1.069	9.066	1.324	1.260	1.322
V_{bus} max dev, worst case [%]	5.164	1.282	10.854	1.509	1.453	1.512
|Mean error of true V_{bus}|, mean [V]	0.50	0.50	14.36	0.51	0.51	0.51
|Mean error of true V_{bus}|, worst [V]	1.05	0.99	38.88	1.08	1.08	1.08
PEM dV/dt, mean ± std [µV/h]	41.93 ± 1.24	42.00 ± 1.23	42.14 ± 1.47	42.12 ± 1.47	42.12 ± 1.47	42.11 ± 1.47
Fraction within ±2%	0.0%	100.0%	26.1%	100.0%	100.0%	100.0%

Table 7. Fraction of realizations of the mismatch set whose maximum V_{bus} deviation stays within a given threshold. * Retuned to $\zeta = 0.707$.

Threshold	PI	PI+FF	IO-FL	IO-FL+I	IO-FL+I *	IDA-PBC
±0.75%	0.0%	27.6%	2.0%	38.7%	42.7%	39.2%
±1%	0.0%	88.9%	8.5%	72.9%	78.4%	72.9%
±1.5%	0.0%	100.0%	16.6%	99.5%	100.0%	99.5%
±2%	0.0%	100.0%	26.1%	100.0%	100.0%	100.0%
±4%	0.0%	100.0%	50.8%	100.0%	100.0%	100.0%
±5%	92.5%	100.0%	63.8%	100.0%	100.0%	100.0%

3.5. Representative Day with Supervisory Start/Stop Operation

Figure 10 shows the cloudy representative day for the five controllers (the retuned variant behaves as IDA-PBC and is omitted), and Table 8 summarizes both days. The supervisory layer starts the stack at 07:52 and stops it four times on the cloudy day (once on the clear day, at dusk); the set-point follows the available PV power up to the 40 A limit,

and the battery charges with the surplus from 50% to 74% (81% on the clear day) without reaching either limit.

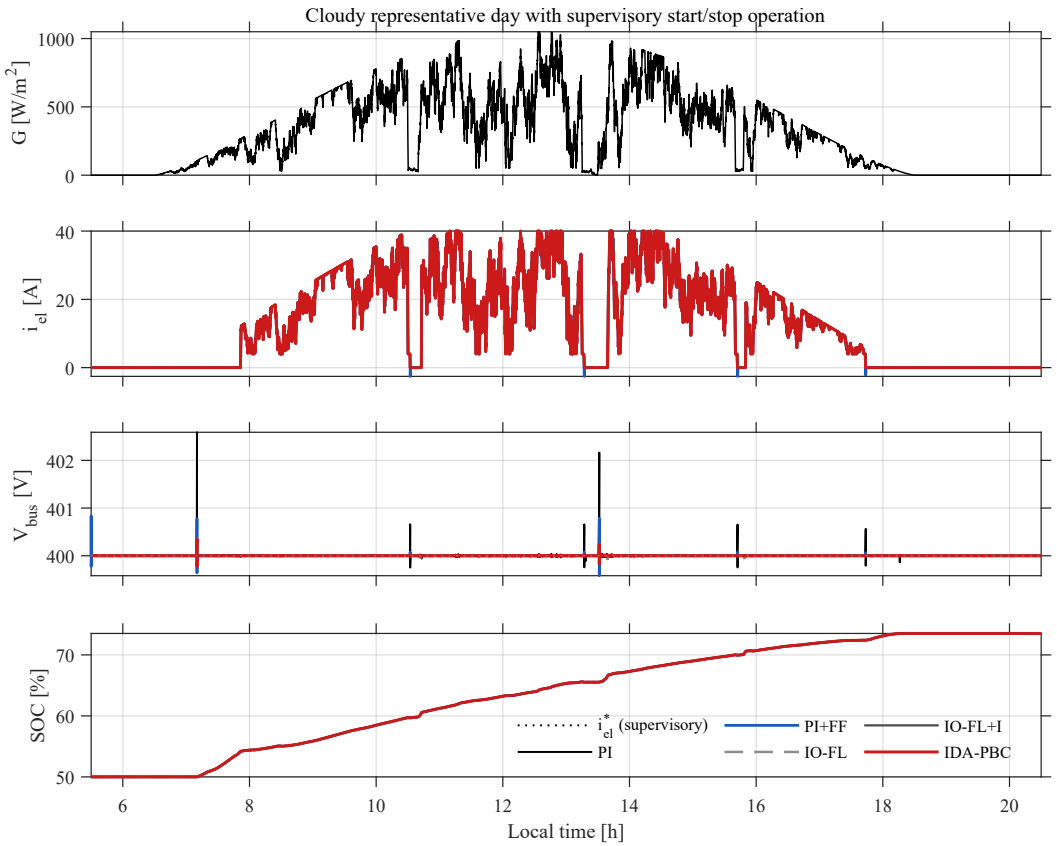


Figure 10. Cloudy representative day with supervisory start/stop operation: irradiance, electrolyzer set-point and current, bus voltage, and battery state of charge for the five controllers. The set-point, the start/stop schedule, and the state-of-charge trajectory are decided by the supervisory layer and are common to all controllers; the controllers differ only in the bus transients at the switching instants. Where the traces coincide, only the IDA-PBC trace, drawn last, is visible.

The quantities that the degradation and economic post-processors use are identical across the five controllers to the precision of the solver: 0.124 equivalent full cycles per day on the cloudy day and 0.157 on the clear day; four and one start/stop cycles, respectively; 0.356 and 0.487 kg of hydrogen; 9.2 and 9.6 h of stack operation; and the same PV energy harvested. This is the expected consequence of placing those decisions in the supervisory layer, and it is the direct evidence for the attribution made in Section 3.6: the controller does not decide how much the battery cycles or how often the stack starts, so it cannot change the degradation terms that depend on those quantities. The Frensch cycling term is active in this scenario, 0.87 µV/h on the cloudy day (four cycles in 9.2 h of stack operation, 0.44 cycles per operating hour, the basis on which the rate is expressed and annualized) and 0.21 µV/h on the clear day (one cycle in 9.6 h), and is the same for all controllers; with the stack held near 60 °C by its thermal management, the thermal term vanishes and the total rate is 5.9 µV/h (5.2 on the clear day), dominated by the baseline. The battery throughput under supervisory operation, 45–57 EFC/yr, is an order of magnitude below the 601 EFC/yr obtained by annualizing the stress window, which is the figure used in Tables 3 and 9; the first-year capacity loss (2.60% on the cloudy day and 2.75% on the clear day, the same for the five controllers to the fourth decimal because it depends only on the throughput, the mean state of charge, and the depth of discharge, all of which the supervisory layer

sets) changes little with respect to the stress scenario (2.51%) because the calendar term dominates, and the projected lifetime remains far outside the economic horizon.

Table 8. Representative day (05:30–20:30) under supervisory operation. Metrics over the whole day excluding the first five minutes. Battery figures are first-year losses with the daily throughput annualized (×365.25); the PEM rate is per hour of stack operation, with the cycling term referred to the hours of stack operation and the stack held near 60 °C.

Day	Metric	PI	PI+FF	IO-FL	IO-FL+I	IDA-PBC	Units
Cloudy	V_{bus} max deviation	0.647	0.197	0.094	0.088	0.088	%
	V_{bus} IAE	31.3	0.055	54.9	0.163	0.163	V·s
	V_{bus} mean error	$<10^{-6}$	$<10^{-7}$	-1.0×10^{-3}	$<10^{-7}$	$<10^{-7}$	V
	Battery EFC per day	0.124	0.124	0.124	0.124	0.124	–
	First-year capacity loss	2.60	2.60	2.60	2.60	2.60	%
	PEM start/stop cycles	4	4	4	4	4	–
	PEM $\mathrm{d}V/\mathrm{d}t$ (cycling term)	5.87 (0.87)	5.87 (0.87)	5.87 (0.87)	5.87 (0.87)	5.87 (0.87)	µV/h
	Hydrogen produced	0.356	0.356	0.356	0.356	0.356	kg
	Stack operating hours	9.19	9.19	9.19	9.19	9.19	h
Clear	V_{bus} max deviation	0.554	0.176	0.083	0.079	0.079	%
	V_{bus} IAE	22.1	0.034	70.5	0.109	0.109	V·s
	Battery EFC per day	0.157	0.157	0.157	0.157	0.157	–
	First-year capacity loss	2.75	2.75	2.75	2.75	2.75	%
	PEM start/stop cycles	1	1	1	1	1	–
	PEM $\mathrm{d}V/\mathrm{d}t$ (cycling term)	5.21 (0.21)	5.21 (0.21)	5.21 (0.21)	5.21 (0.21)	5.21 (0.21)	µV/h
	Hydrogen produced	0.487	0.487	0.487	0.487	0.487	kg

Regulation differs between controllers only at the switching events. The largest bus excursion of the day occurs at the instants at which the supervisory layer enables the PV converter from open circuit, at 07:10 and again at 13:31 after the deepest cloud passage has disabled it: 2.6 V (0.65%) for PI, 0.79 V for PI+FF, 0.38 V for IO-FL, and 0.35 V for IO-FL+I and IDA-PBC. The electrolyzer start/stop events are much smaller disturbances: the start, ramped at 2 A/s, is invisible on the bus (below 0.03 V for every controller), and the stop, which cuts the 4 A minimum current at once, produces 0.66 V for PI, 0.08 V for PI+FF, and at most 0.11 V for the model-based variants. The slow irradiance variations of the day, including the three deep cloud passages, are followed by the PV-following set-point and absorbed by the battery with sub-volt excursions in all cases. Two differences with the stress scenario deserve comment. First, the model-based variants have a smaller peak than PI+FF here, whereas PI+FF has the smaller peak under abrupt cloud drop-outs: the dominant disturbance of the day is a switching transient that the exact cancellation of the inner loops handles better, while the dominant disturbance of the stress scenario is an irradiance step for which the PI inner loops with their integrators recover faster. Second, the IAE of the canonical IO-FL accumulates over fifteen hours to 55–70 V·s from a mean offset of only 1 mV, which is a reminder that this metric penalizes the absence of integral action in proportion to the window length rather than to any excursion of practical relevance. All five controllers keep the bus within ±0.7% throughout both days.

3.6. Component Aging Analysis

Long-term degradation of the battery and PEM electrolyzer is evaluated by extrapolating the rates observed under stress conditions to annual values, using the Naumann LFP model [14,15] for the battery and the Frensch model [10] for the PEM stack. The consolidated results are presented in Table 9 for the three original controllers; the three ablation variants fall within the same ranges (Table 3) and are omitted for brevity. The

representative day of Section 3.5 provides the complementary view under supervisory operation.

Battery aging is dominated by the calendar component (2.12% in the first year, 84.6% of the total), driven by storage temperature and mean state of charge, both architectural rather than controller-dependent quantities. The cycle component is the same for all strategies to the fourth decimal, and the projected time to 80% remaining capacity is 63.5 years for all controllers. These figures assume that the stress-window throughput (601 EFC/yr) continues around the clock; under the supervisory operation of the representative day, the battery only buffers the PV–electrolyzer mismatch and the throughput is 0.12–0.16 EFC per day (45–57 EFC/yr), which shifts the projected life upward but, again, identically for all controllers (Section 3.5).

Table 9. Component aging extrapolated from the stress scenario under continuous operation (8766 h/yr). Battery figures are first-year losses of the $\sqrt{t}$ model, not constant rates. EOL denotes the end-of-life condition: 80% remaining capacity for the battery and a +10% stack voltage for the PEM.

Component	Metric	PI	IO-FL	IDA-PBC	Units
Battery (Naumann LFP)					
	Calendar capacity loss	2.123	2.123	2.123	%/yr
	Cycle capacity loss	0.387	0.387	0.387	%/yr
	Total capacity loss	2.509	2.509	2.509	%/yr
	Projected years to 80%	63.52	63.52	63.52	years
PEM electrolyzer (Frensch)					
	Voltage degradation rate	42.21	42.21	42.21	µV/h
	V_{el} loss per year	0.3700	0.3700	0.3700	V
	Efficiency loss	0.385	0.385	0.385	%/yr
	Projected years to EOL	25.95	25.95	25.95	years

These figures are $\sqrt{t}/\sqrt{\mathrm{EFC}}$ extrapolations of the stress-window degradation under controlled laboratory conditions and exceed realistic field lifetimes; they are reported only to confirm that the aging-based end of life is non-binding, with the 10-year calendar cap of Section 2.8.4 governing the replacement schedule in every scenario.

PEM aging shows no controller dependence at the precision of the table: although the model-based variants suppress the electrolyzer ripple to numerical zero, the ripple term contributes at most 0.003 µV/h for PI on a 42 µV/h total, so the projected efficiency loss (0.385%/yr) and end of life (25.95 years) coincide for the six controllers to three significant figures. The structure of the Frensch model (Equation (35)) explains this result: only the ripple term depends on the controller, while the baseline rate and the thermal contribution (mean stack temperature above T_{ref}) are set by the operating profile and the thermal management. Together, these account for more than 99% of the total degradation in the stress scenario, where the ON/OFF cycling term is inactive; the thermal term alone contributes 37 of the 42 µV/h because the stack, uncooled in that window, averages 79 °C, whereas with the thermal management of the representative day, it stays near 60 °C and the rate falls to 5.2–5.9 µV/h (Section 3.5). The absolute rate is thus set by the thermal design, not by the controller. This last point bounds the scope of the stress-scenario result: start/stop cycling is an important degradation mechanism in real off-grid PV–electrolyzer systems, and the constant set-point switches it off. The representative day of Section 3.5 restores it; there, the cycling term is non-zero and, because the start/stop schedule is decided by the supervisory layer from the irradiance, it is the same for all controllers: four cycles on the cloudy day and one on the clear day, contributing 0.87 and 0.21 µV/h per hour of stack operation, respectively (Table 8). The conclusion that controller choice has a negligible influence on PEM lifetime therefore holds both for continuously operated

systems and for systems whose start/stop decisions are taken, as is usual, above the converter-level controller; it does not extend to supervisory strategies that differ in their cycling behavior, which are outside the scope of this comparison. The battery buffer further shields the electrolyzer current from bus transients, independently of the controller used.

Component lifetime in this system is therefore governed by the architectural decision of incorporating a battery buffer and by the supervisory layer rather than by the converter-level control strategy; the value of the model-based laws lies in regulation quality, compliance with the regulation target, and robustness (Sections 3.1–3.4), not in lifetime extension.

3.7. Economic Analysis: Levelized Cost of Hydrogen

Under the base-case assumptions of Table 2, the LCOH is 29.972 USD/kg H_2 for each of the six controllers; the values coincide to the fourth decimal (relative spread below 10^{-4}%) because the quantities that feed the economic model—hydrogen production, battery throughput, and the aging projections—are the same for all of them. Figure 11 shows the breakdown: capital expenditure represents 80.6% (24.16 USD/kg) and operating expenditure represents 19.4% (5.81 USD/kg); no replacement falls inside the horizon. For reference, the alternative convention that charges the year-10 replacement of both components in full and credits no residual value gives 34.20 USD/kg with the same spread (Table 10): a replacement at the end of the horizon provides no production within it, and its full cost inflates the absolute figure by 4.2 USD/kg without affecting the comparison.

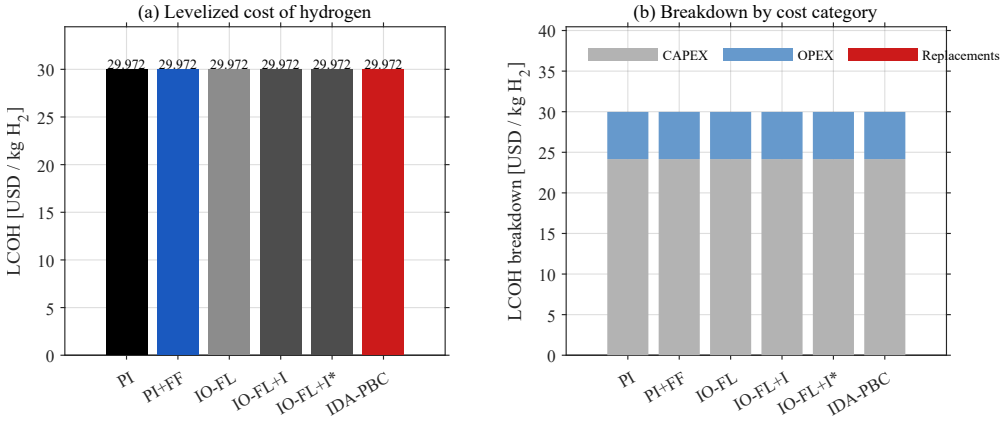


Figure 11. LCOH breakdown by cost category for the six controllers (base case). The cost structures are identical (29.972 USD/kg for every controller). IO-FL+I*: IO-FL+I retuned to $\zeta = 0.707$.

Within the 10-year project horizon, no controller triggers a replacement. The aging-based end-of-life projections, now annualized with the 2400 h/yr operating schedule, are ∼74 years for the battery and ∼95 years for the PEM stack for all six controllers (Table 3 gives the corresponding 26-year PEM figure under the continuous-operation basis); the 10-year calendar cap is therefore the binding criterion, and the replacement schedule is controller-independent by construction. This is a limitation of what the economic comparison can resolve, not a result: a controller could only change the LCOH through replacements if its aging projection fell inside the horizon, and none does, with or without the cap. To make this explicit, Table 10 includes a variant in which replacement is governed solely by the aging models with no calendar limit, for the 10- and 20-year horizons; the LCOH is unchanged at 10 years and lower at 20 years, with the controller spread unaffected in both. Hydrogen production computed from the simulated current is 132.31 kg/yr for all six controllers; the tracking differences between controllers are below 10^{-4} in relative terms and do not register in the LCOH. The PEM efficiency loss reduces the present value of cumulative production by ≈0.6% over the horizon under the operating-hour basis.

The obtained LCOH of ∼30 USD/kg lies far above the utility-scale Atacama benchmarks of 2.12 USD/kg [17] and 3.67–4.69 USD/kg [18], consistent with the small-scale off-grid nature of the system: unit costs are 1.5–3× higher, operating hours are lower without tracking, and economies of scale on balance of plant are absent. The analysis is therefore representative of remote applications where the architecture is valued for autonomy and reliability rather than cost minimization.

The robustness of the base-case result is tested against alternative scenarios spanning the dominant uncertainty axes of the economic model (Section 2.8.4), the replacement convention, and the battery size (Section 3.8). The results are summarized in Table 10 and visualized as a tornado plot in Figure 12.

Table 10. LCOH base case and sensitivity scenarios (USD/kg). The six controllers give the same value in every scenario (relative spread below 10^{-4}%), so a single column is reported. "Aging only" removes the 10-year calendar cap so that replacement is governed solely by the degradation models.

Scenario	LCOH, All Six Controllers
Base case (WACC 7%, 10 yr, 2400 h/yr)	29.972
Base case, aging-only replacement	29.972
Year-10 replacement charged in full, no residual value	34.204
CAPEX −30% (optimistic)	21.451
CAPEX +30% (pessimistic)	38.493
WACC 5%	27.792
WACC 10%	33.420
Horizon 15 years	26.594
Horizon 20 years	24.724
Horizon 20 years, aging-only replacement	21.908
Operation 3500 h/yr (Atacama prime)	20.618
Battery 5 kWh (cost side)	26.600
Battery 15 kWh (cost side)	33.035
Battery 20 kWh (cost side)	36.252

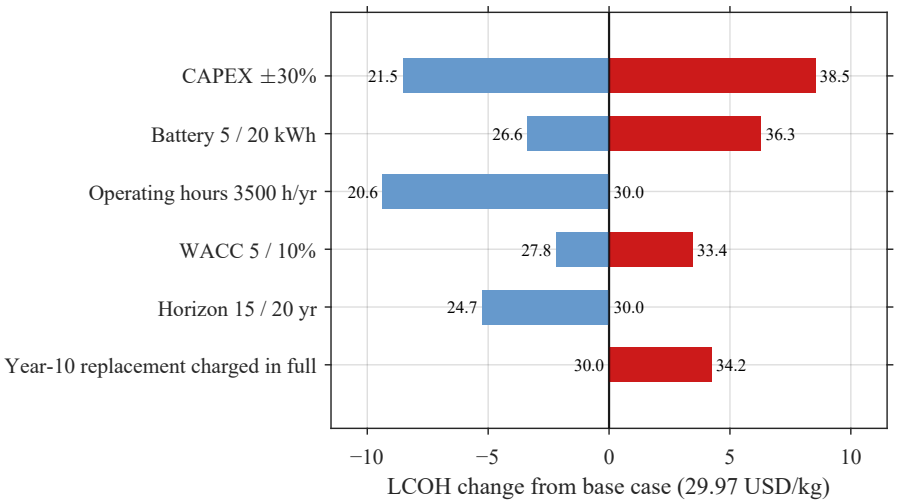


Figure 12. Tornado plot of LCOH sensitivity to the economic and operating parameters and to the battery size. The vertical line marks the base-case LCOH (29.97 USD/kg). Blue bars indicate a decrease and red bars an increase in the LCOH with respect to the base case. Capital expenditure dominates the uncertainty range, followed by battery size, operating hours, discount rate, and project horizon.

Three findings stand out. First, CAPEX is the dominant axis: a ±30% perturbation produces an LCOH range of 21.45–38.49 USD/kg, consistent with its 80.6% share of the base-case composition; increasing operation to 3500 h/yr (single-axis tracking) reduces

the LCOH by 31%, while horizon and WACC have smaller effects (−11% to −18% and −7% to +12%, respectively). Battery size moves the LCOH by −11% to +21% over the 5–20 kWh range on the cost side alone; Section 3.8 examines whether it also changes the regulation ranking.

Second, and most relevant to this work, the controller ranking is preserved in every scenario, but the absolute spread remains in the third decimal of USD/kg, against a typical literature precision of ±0.5 USD/kg for cost components alone [17,18]. The spread is bounded by construction in the base case, since no controller triggers a replacement, and it stays equally small when the cap is removed, when the horizon is extended to 20 years, and when the end-of-horizon replacement is charged in full. Controller selection therefore has no economic significance within the precision of the LCOH analysis itself: the choice of a control law must be justified on operational grounds.

Third, the analysis addresses the potential trade-off between regulation performance and hydrogen yield [7,36]: since the six controllers track the 30 A set-point with negligible steady-state error, the production computed from the simulated current is equal across controllers to four significant figures (132.31 kg/yr), and the only controller-induced variation appears in the second-order PEM degradation term. The regulation improvement of the feed-forward variants comes without any penalty on hydrogen yield or efficiency.

3.8. Sensitivity of the Regulation Ranking to Battery Size

Table 11 repeats the stress scenario with 25, 50, and 100 Ah packs (5.1, 10.2, and 20.5 kWh at 204.8 V), with the pack internal resistance scaled inversely with capacity and all controller gains unchanged. The regulation ranking is the same at the three sizes: PI+FF has the smallest peak deviation (0.67, 0.65, 0.63%) and IAE, the four model-based variants follow within 0.84–0.91%, and PI stays at 4.6%. The peak metrics are almost insensitive to the pack size because the bus transient is governed by the bus capacitor and the current-loop bandwidth, not by the battery impedance, and the battery current demanded by the feed-forward is the same power-balance correction whatever the pack behind it. On the aging side, the smaller pack cycles twice as deeply in relative terms (1192 against 302 EFC/yr under the stress annualization) and its first-year loss rises from 2.38 to 2.71%, identically for all controllers. Battery size therefore moves the absolute lifetime and the LCOH (Table 10) but not the controller ranking or the controller neutrality of degradation, which answers the sizing question in the affirmative within the range tested; ratios outside it, in particular packs too small to absorb the PV–electrolyzer imbalance without hitting their current limit, would require the supervisory layer to curtail and are outside the present comparison.

Table 11. Stress scenario with three battery sizes (internal resistance scaled as $1/Q_{nom}$). Battery aging under the continuous-operation annualization for comparability with Table 3. * Retuned to $\zeta = 0.707$.

Pack	Metric	PI	PI+FF	IO-FL	IO-FL+I	IO-FL+I *	IDA-PBC
25 Ah	V_{bus} max dev [%]	4.596	0.669	0.908	0.885	0.840	0.885
	V_{bus} IAE [V·s]	4.65	0.115	15.57	0.588	0.414	0.588
	First-year loss [%]/EFC/yr	2.71 / 1192 (all controllers)					
50 Ah	V_{bus} max dev [%]	4.574	0.646	0.907	0.884	0.840	0.884
	V_{bus} IAE [V·s]	4.67	0.092	15.82	0.587	0.414	0.588
	First-year loss [%]/EFC/yr	2.51 / 601 (all controllers)					
100 Ah	V_{bus} max dev [%]	4.565	0.634	0.907	0.884	0.839	0.884
	V_{bus} IAE [V·s]	4.69	0.087	15.95	0.587	0.413	0.587
	First-year loss [%]/EFC/yr	2.38 / 302 (all controllers)					

3.9. Computational Burden and Actuator Saturation

All simulations use the stiff solver `ode23tb` of MATLAB R2024b with the tolerances of Section 2.8 on a four-core laptop processor (Intel Core, 11th generation). Table 12 gives the wall-clock times. The 600 s stress window takes 7.5–10 s for every controller (13,400–15,000 accepted steps). One realization of the first Monte Carlo set takes 3–4 s per controller, and one of the mismatch set takes 17–42 s because the band-limited measurement error forces smaller steps, most noticeably for the model-based laws, which feed the corrupted measurements through the nonlinear cancellation. The 15 h representative day takes 3–27 min per controller (550,000–700,000 steps), the longest being the canonical IO-FL on the cloudy day. The Monte Carlo and daily runs were executed in three concurrent MATLAB instances, so their times include contention. The control law itself is a negligible part of this cost: one evaluation takes 32 µs for the PI cascade, 53 µs for PI+FF, and 99–119 µs for the four model-based laws in interpreted MATLAB (averaged over 10^4 calls), including the evaluation of the electrolyzer polarization model that the latter require; the model-based laws therefore cost about three times the PI cascade, a difference without practical consequence at the 1 kHz control rate used.

Table 12. Wall-clock simulation time per controller (MATLAB R2024b, `ode23tb`, four-core laptop processor). Monte Carlo figures are means over the realizations; the daily runs exclude the retuned variant, which was not simulated in that scenario. * Retuned to $\zeta = 0.707$.

Scenario	PI	PI+FF	IO-FL	IO-FL+I	IO-FL+I *	IDA-PBC	Units
Stress scenario (600 s)	9.8	7.5	8.1	9.4	8.0	7.5	s
Monte Carlo, plant variation, per realization	3.4	3.7	4.4	4.4	4.3	4.2	s
Monte Carlo, model mismatch, per realization	17.3	22.9	42.4	42.2	42.3	41.2	s
Cloudy representative day (15 h)	11.3	14.0	27.2	19.9	–	11.2	min
Clear representative day (15 h)	9.4	2.6	8.4	6.0	–	6.0	min
One control-law evaluation	32	53	101	119	102	99	µs

No actuator limit is reached in any deterministic scenario. Re-evaluating the six control laws along the stored trajectories shows that the three duty cycles stay inside their limits with margin (PV boost 0.28–0.54, battery converter 0.47–0.57, electrolyzer buck 0.13–0.25 while the stack is on), that the battery-current reference peaks at 18.3 A (PI+FF, stress scenario) against its ± 100 A limit, that the PV-current reference never reaches its upper bound, and that, consequently, the anti-windup logic of the PI family and the integral anti-windup of IO-FL+I and IDA-PBC are never engaged in the stress scenario or in either representative day. The same holds at the switching instants of the supervisory layer, where the largest transients of the day occur. Saturation was not monitored in the Monte Carlo sets, whose trajectories are not stored; the deviations observed there (the transients of the PI cascade and the steady-state offset of the canonical IO-FL) are of the same kind and size as in the stress scenario, where no limit is active.

4. Discussion

Taken together, the results give a fuller picture of the role of advanced nonlinear control in off-grid green hydrogen systems, organized around (i) architecture-versus-controller attribution of system-level outcomes, (ii) practical guidance for controller selection, and (iii) positioning relative to the literature.

4.1. Architecture Versus Control Attribution

The central finding is a clear separation between the operational and lifecycle benefits of control design, together with a precise attribution of the former. On the operational

side, the controllers that embed the power-balance feed-forward reduce the maximum V_{bus} deviation 5–7-fold, meet the $\pm 2\%$ target across $N = 200$ perturbed plants, and suppress the electrolyzer ripple to numerical precision. The ablation study shows that this is the work of the feed-forward: a PI cascade with that single term added (PI+FF) outperforms IDA-PBC on every regulation metric in every realization, and IDA-PBC itself coincides with IO-FL plus an integrator on this plant. What the port-Hamiltonian route adds is not performance but a stability certificate for the slow dynamics and a physical interpretation of the gains, which is a legitimate reason to prefer it when a certificate is required, provided its assumptions are stated (Section 2.6.3). Under model mismatch and measurement error (Section 3.4), the picture simplifies further: the four variants that combine the feed-forward with integral action converge to the same band (0.83–0.86% mean peak deviation, 100% compliance), the canonical IO-FL fails the target in three realizations out of four because of its steady-state offset, and PI fails it in all.

On the lifecycle side, the six controllers produce the same component lifetimes and the same LCOH (29.972 USD/kg, coincident to the fourth decimal). This decoupling persists across $\pm 30\%$ CAPEX variations, factor-of-two WACC ranges, horizons of 10 to 20 years, replacement governed by the calendar cap or by the aging models alone, battery sizes from 5 to 20 kWh, and the full Monte Carlo set. Part of it is structural and is stated as such: within a 10-year horizon, no controller reaches an aging-based end of life, so the replacement schedule cannot differ between controllers whatever the convention. The rest is physical: the battery buffer absorbs the PV–electrolyzer power imbalance and isolates the PEM stack from bus transients regardless of the upstream controller, and the supervisory layer, not the converter-level controller, decides the throughput of the battery and the start/stop count of the stack. The representative day makes this explicit: the five controllers produce the same 0.12 EFC per day, the same four start/stop cycles, and the same 0.356 kg of hydrogen on the cloudy day and differ only in sub-volt bus transients at the switching instants. Calendar aging (driven by temperature and mean state of charge, both architectural choices) accounts for 84.6% of the first-year battery capacity loss, while PEM degradation is dominated by the baseline rate and the thermal term; the ripple-dependent term that model-based control suppresses is, by construction, the smallest contribution when the battery is sized to absorb power imbalances.

Five caveats bound the scope of these findings. First, the averaged plant omits the PWM ripple at f_{sw} = 20 kHz by design. From analytical converter ripple expressions, we expect it to add $\approx$0.4–0.6 μV/h to the Frensch baseline, and we assume that this contribution is the same for all controllers because it is set by the converter design rather than by the outer control law, as the ripple reductions obtained with interleaved topologies illustrate [53,54]; both the magnitude and the controller independence are assumptions pending a switched-model or hardware-in-the-loop study, not results of this work. The near-zero loop ripple of the model-based variants indicates near-perfect tracking within the averaged model, not a physical ripple level. Second, the aging models are used as published; their validation covers the source cells and stacks, not this pack, stack, and profile, so the absolute lifetimes are model extrapolations and only the cross-controller comparison is claimed. Third, the supervisory layer of the representative day is a simple PV-following scheme with hysteresis; supervisory strategies that cycle the stack differently would change the absolute PEM degradation for all controllers alike, but a comparison of supervisory strategies is a different study. Fourth, the model parameters correspond to representative commercial-grade components at the 4–10 kW scale rather than to a specific experimental setup; experimental validation is left for future work. Fifth, the representative days are synthetic daylight profiles. They exercise start/stop operation and PV-following set-points, but they do not establish annual performance under seasonal

variability, overnight operation, prolonged energy shortages, or active state-of-charge limits, which were never reached in the simulated days. The lifecycle and economic conclusions are therefore restricted to the investigated architecture, the shared supervisory strategy, and the operating scenarios simulated; an annual simulation with an energy-management layer that activates the state-of-charge limits would be needed to extend them.

With these caveats, the results revise the usual case made for advanced control in renewable hydrogen systems [31,33,36]: for a battery-buffered system operated under a shared supervisory strategy, in the scenarios simulated here, the claim that advanced nonlinear control extends component life or reduces cost is not supported quantitatively, and the regulation benefit that is real can be obtained by adding a model-based feed-forward to a conventional cascade. The value of the nonlinear design routes lies in the stability certificate and in the systematic way they arrive at that feed-forward.

4.2. Practical Guidance for Controller Selection

The ablation results turn the selection question into a question about which elements of the design are needed. A plain PI cascade remains appropriate where the regulation tolerance is loose (>±5%), the site is accessible, and simplicity with minimal computational footprint outweighs dynamic performance. Whenever a tighter target applies, the first element to add is the power-balance feed-forward: it requires the measured PV and electrolyzer currents, the duty cycles, and the battery voltage, all of which are available in any implementation, and it brings a PI cascade to 0.65% peak deviation and 100% compliance with the ±2% target on this system; under model mismatch and sensor error, it keeps the target in every realization, with a worst case of 1.3%, and is statistically indistinguishable from IDA-PBC. The canonical IO-FL offers the same peak suppression but should not be deployed without integral action: its exact-cancellation structure leaves a steady-state offset under any parameter mismatch, and in the mismatch Monte Carlo, it misses the ±2% target in 74% of the realizations, with offsets of up to 39 V. IO-FL with an integrator and IDA-PBC are the same law and share the same performance; IDA-PBC is the design route to prefer when a Lyapunov certificate is required, for instance, for the integration of multiple parallel converters on a common DC bus, where the energy-based formulation facilitates system-level stability analysis, with the scope of that certificate stated as in Section 2.6.3. The off-grid Atacama application that motivates this study requires tight regulation under disturbances and robustness to parameter variation in series-produced units; according to the evidence in this paper, those requirements are met by PI+FF, and the port-Hamiltonian design is justified by the certificate rather than by the numbers.

4.3. Comparison with the Literature

The present work intersects three streams that have evolved largely in isolation. In the control-comparison literature, Ali et al. [25] benchmark MPC against PI and sliding mode, Csizmadia et al. [31] apply feedback linearization to an electrolyzer-feeding converter, Roy et al. [28] validate higher-order sliding mode in hardware-in-the-loop, and Abdolmaleki et al. [33] apply IDA-PBC to DC–DC converters and isolated networks—all without aging or economic evaluation. Our study supplies what they lack: a comparative control study combined with published degradation models and an economic post-processor. On the techno-economic side, the Atacama benchmarks of Gallardo et al. [18] and Armijo and Philibert [17] correspond to utility-scale plants; the order-of-magnitude gap with the ∼30 USD/kg obtained here reflects scale and off-grid operation rather than methodology and characterizes a cost regime (remote off-grid production) not previously detailed in the literature. In the uncertainty-analysis stream, Ginsberg et al. [7] apply Monte Carlo methods to off-grid solar hydrogen without comparing controllers; the present analysis

closes this gap with two sets of $N = 200$ paired realizations across six controllers, one with the controllers retuned to each plant and one with nominal controllers facing model and measurement error, showing which elements of the design carry the operational ranking over the uncertainty envelope while the economic differences remain practically negligible. The order-of-magnitude gap with the utility-scale benchmarks does not depend on the replacement convention ($\sim$30 USD/kg in the base case, $\sim$34 when the end-of-horizon replacement is charged in full).

5. Conclusions

This work presented a comparative analysis of PI cascade, IO-FL, and IDA-PBC controllers, together with three ablation variants, for the converter-level control of an off-grid PV–battery–PEM electrolyzer system for green hydrogen production. The controllers were tuned to matched closed-loop bandwidth specifications and evaluated under a unified framework: a seven-state averaged plant, a deterministic stress scenario, two sets of $N = 200$ paired Monte Carlo realizations (plant variation with retuned controllers and model mismatch with measurement error), a representative day with supervisory start/stop operation, the Naumann LFP and Frensch PEM degradation models, and an NPV-based LCOH analysis. The economic analysis includes sensitivity to CAPEX, WACC, project horizon, operating hours, replacement convention, and battery size.

On this plant, the IDA-PBC law coincides, on the slow bus-voltage manifold, with IO-FL augmented by an integrator, and the regulation benefit of both is explained by the model-based power-balance feed-forward they share. Adding that feed-forward to the PI cascade reduces the maximum DC bus-voltage deviation from 4.57% to 0.65%, below the 0.88% of IDA-PBC, and does so in every one of 200 perturbed plants; integral action, not the nonlinear structure, sets the accumulated-error ranking, and retuning IDA-PBC to the common damping ratio does not alter these conclusions. When the controllers operate with nominal models and corrupted measurements, the four variants that combine the feed-forward with integral action keep the $\pm$2% target in every one of 199 realizations and become statistically indistinguishable, the canonical IO-FL misses it in three realizations out of four, and PI misses it in all. By contrast, for the investigated architecture, supervisory strategy, and operating scenarios, the six controllers produce the same component lifetimes and the same LCOH (29.972 USD/kg, coincident to the fourth decimal, with CAPEX accounting for 80.6% of the cost), results that persist across all sensitivity scenarios, with replacement governed by the calendar cap or by the aging models alone, and across both Monte Carlo sets; under supervisory operation, the battery throughput and the PEM start/stop count are the same for all controllers because they are decided by the supervisory layer.

The principal methodological contribution is the explicit attribution of system-level outcomes: architectural decisions (battery buffer sizing, calendar lifetime assumptions) and the supervisory layer (set-point, start/stop, state-of-charge management) govern the lifecycle and economic metrics in the scenarios investigated, whereas the converter-level controller determines regulation quality, and within the controller, it is the feed-forward and the integrator, not the design route, that determine it. The adoption of IDA-PBC is therefore justified by the stability certificate it provides and by the systematic derivation of the control law, not by better regulation than a well-designed cascade and not by cost minimization; practical selection guidance across deployment contexts is given in Section 4.2. Future work will extend the comparison to model predictive control and to supervisory strategies with different cycling behavior; run annual simulations with seasonal variability, overnight operation, and active state-of-charge limits; incorporate battery thermal dynamics and PV degradation; address the PWM-frequency contribution through switched-model simulation;

validate the findings experimentally on a laboratory-scale system; and assess scalability to medium-scale and grid-connected installations.

Author Contributions: Conceptualization, R.F., A.S.-S., and A.B.; methodology, R.F., A.S.-S., A.B., and D.S.; software, R.F. and A.B.; validation, A.S.-S., D.S., F.Y., and R.B.; formal analysis, R.F., A.S.-S., and A.B.; investigation, R.F., A.B., D.S., F.Y., and R.B.; resources, A.S.-S.; data curation, R.F.; writing—original draft preparation, R.F., A.S.-S., A.B., and D.S.; writing—review and editing, R.F., A.B., D.S., F.Y., and R.B.; visualization, R.F., A.S.-S., D.S., F.Y., and R.B.; supervision, A.S.-S.; project administration, A.B. All authors have read and agreed to the published version of the manuscript.

Funding: This research received no external funding. The APC was funded by Universidad Técnica Federico Santa María.

Institutional Review Board Statement: Not applicable.

Informed Consent Statement: Not applicable.

Data Availability Statement: The MATLAB source code, the parameter files, the random seeds, and the data behind every table and figure of this article are openly available in Zenodo at https://doi.org/10.5281/zenodo.23632405 (version 2.0.1 corresponds to this article; version 1.0.0 corresponds to the originally submitted version).

Acknowledgments: A. Sánchez-Squella was supported by a research grant from the National Research and Development Agency (ANID) CTI 250019 Innovation Center for Sustainable Energy Transition (SET-Chile) and FONDEF IDEA I+D 2026 ID26 I 10691. A. Barrueto thanks ANID for its support through the Fondecyt de Iniciación en Investigación 2026 project (No. 11260377) and Fondef IDEA project (No. ID26I10691). R. Flores acknowledges the support of ANID/Scholarship Program/Beca de Doctorado Nacional/2026-21262898.

Conflicts of Interest: The authors declare that they have no known competing financial interests or personal relationships that could have appeared to influence the work reported in this paper.

Abbreviations

The following abbreviations are used in this manuscript:

CAPEX	Capital expenditure
DOD	Depth of discharge
ECDF	Empirical cumulative distribution function
EFC	Equivalent full cycles
EMS	Energy management system
EOL	End of life
IAE	Integral of absolute error
IDA-PBC	Interconnection and damping assignment passivity-based control
IO-FL	Input–output feedback linearization
ITAE	Integral of time-weighted absolute error
LCOH	Levelized cost of hydrogen
LFP	Lithium iron phosphate
MPC	Model predictive control
MPPT	Maximum power point tracking
NPV	Net present value
O&M	Operation and maintenance
OPEX	Operating expenditure
PCH	Port-controlled Hamiltonian
PEM	Proton exchange membrane
PI	Proportional–integral
PV	Photovoltaic
PWM	Pulse width modulation

RMS	Root mean square
SOC	State of charge
STC	Standard test conditions
WACC	Weighted average cost of capital

References

1. Turner, J.A. Sustainable hydrogen production. *Science* **2004**, *305*, 972–974. [CrossRef] [PubMed]
2. IEA. *Global Hydrogen Review 2023*; Technical report; International Energy Agency: Paris, France, 2023. Available online: https://www.iea.org/reports/global-hydrogen-review-2023 (accessed on 1 October 2026).
3. Molina, A.; Falvey, M.; Rondanelli, R. A solar radiation database for Chile. *Sci. Rep.* **2017**, *7*, 14823. [CrossRef] [PubMed]
4. IRENA. *Renewable Power Generation Costs in 2024*; Technical report; International Renewable Energy Agency: Abu Dhabi, United Arab Emirates, 2024.
5. Toghyani, S.; Baniasadi, E.; Afshari, E. Performance assessment of an electrochemical hydrogen production and storage system for solar hydrogen refueling station. *Int. J. Hydrogen Energy* **2021**, *46*, 24271–24285. [CrossRef]
6. Ursua, A.; Gandia, L.M.; Sanchis, P. Hydrogen production from water electrolysis: Current status and future trends. *Proc. IEEE* **2011**, *100*, 410–426. [CrossRef]
7. Ginsberg, M.J.; Esposito, D.V.; Fthenakis, V.M. Designing off-grid green hydrogen plants using dynamic polymer electrolyte membrane electrolyzers to minimize the hydrogen production cost. *Cell Rep. Phys. Sci.* **2023**, *4*, 101625. [CrossRef]
8. Maoulida, F.; Guilbert, D.; Camara, M.B.; Dakyo, B. Dynamic electrical degradation of PEM electrolyzers under renewable energy intermittency: Mechanisms, diagnostics, and mitigation strategies–A comprehensive review. *Renew. Sustain. Energy Rev.* **2026**, *225*, 116170. [CrossRef]
9. Wang, C.R.; Stansberry, J.M.; Mukundan, R.; Chang, H.M.J.; Kulkarni, D.; Park, A.M.; Plymill, A.B.; Firas, N.M.; Liu, C.P.; Lang, J.T.; et al. Proton Exchange Membrane (PEM) Water Electrolysis: Cell-Level Considerations for Gigawatt-Scale Deployment. *Chem. Rev.* **2025**, *125*, 1257–1302. [CrossRef] [PubMed]
10. Frensch, S.H.; Fouda-Onana, F.; Serre, G.; Thoby, D.; Araya, S.S.; Kær, S.K. Influence of the operation mode on PEM water electrolysis degradation. *Int. J. Hydrogen Energy* **2019**, *44*, 29889–29898. [CrossRef]
11. Rakousky, C.; Reimer, U.; Wippermann, K.; Carmo, M.; Lueke, W.; Stolten, D. An analysis of degradation phenomena in polymer electrolyte membrane water electrolysis. *J. Power Sources* **2016**, *326*, 120–128. [CrossRef]
12. Parra, D.; Valverde, L.; Pino, F.J.; Patel, M.K. A review on the role, cost and value of hydrogen energy systems for deep decarbonisation. *Renew. Sustain. Energy Rev.* **2019**, *101*, 279–294. [CrossRef]
13. Ecker, M.; Nieto, N.; Käbitz, S.; Schmalstieg, J.; Blanke, H.; Warnecke, A.; Sauer, D.U. Calendar and cycle life study of Li(NiMnCo)O_2-based 18650 lithium-ion batteries. *J. Power Sources* **2014**, *248*, 839–851. [CrossRef]
14. Naumann, M.; Schimpe, M.; Keil, P.; Hesse, H.C.; Jossen, A. Analysis and modeling of calendar aging of a commercial LiFePO4/graphite cell. *J. Energy Storage* **2018**, *17*, 153–169. [CrossRef]
15. Naumann, M.; Spingler, F.B.; Jossen, A. Analysis and modeling of cycle aging of a commercial LiFePO4/graphite cell. *J. Power Sources* **2020**, *451*, 227666. [CrossRef]
16. Valente, A.; Iribarren, D.; Dufour, J. Life cycle assessment of hydrogen energy systems: A review of methodological choices. *Int. J. Life Cycle Assess.* **2017**, *22*, 346–363. [CrossRef]
17. Armijo, J.; Philibert, C. Flexible production of green hydrogen and ammonia from variable solar and wind energy: Case study of Chile and Argentina. *Int. J. Hydrogen Energy* **2020**, *45*, 1541–1558. [CrossRef]
18. Gallardo, F.I.; Ferrario, A.M.; Lamagna, M.; Bocci, E.; Garcia, D.A.; Baeza-Jeria, T.E. A Techno-Economic Analysis of solar hydrogen production by electrolysis in the north of Chile and the case of exportation from Atacama Desert to Japan. *Int. J. Hydrogen Energy* **2021**, *46*, 13709–13728. [CrossRef]
19. U.S. Department of Energy. *Pathways to Commercial Liftoff: Clean Hydrogen*; Technical Report Liftoff Report; U.S. Department of Energy: Washington, DC, USA, 2024.
20. Viswanathan, V.; Mongird, K.; Franks, R.; Li, X.; Sprenkle, V.; Baxter, R. *2022 Grid Energy Storage Technology Cost and Performance Assessment*; Technical Report PNNL-33283; Pacific Northwest National Laboratory: Richland, WA, USA, 2022.
21. Morstyn, T.; Savkin, A.V.; Hredzak, B.; Agelidis, V.G. Multi-agent sliding mode control for state of charge balancing between battery energy storage systems distributed in a DC microgrid. *IEEE Trans. Smart Grid* **2017**, *9*, 4735–4743. [CrossRef]
22. Sánchez-Squella, A.; Ortega, R.; Griño, R.; Malo, S. Dynamic energy router. *IEEE Control Syst. Mag.* **2010**, *30*, 72–80. [CrossRef]
23. Morales, F.; Cisneros, R.; Ortega, R.; Sánchez-Squella, A. Nonlinear voltage regulation of an auxiliary energy storage of a multiport interconnection. *arXiv* **2024**, arXiv:2403.19901.

24. Fernández, F.J.V.; Segura Manzano, F.; Andújar Márquez, J.M.; Calderón Godoy, A.J. Extended model predictive controller to develop energy management systems in renewable source-based smart microgrids with hydrogen as backup. Theoretical foundation and case study. *Sustainability* **2020**, *12*, 8969. [CrossRef]
25. Ali, S.U.; Waqar, A.; Aamir, M.; Mian Qaisar, S.; Iqbal, J. Model predictive control of consensus-based energy management system for DC microgrid. *PLoS ONE* **2023**, *18*, e0278110. [CrossRef] [PubMed]
26. Zidane, N.; Belaid, S.L. A new fuzzy logic solution for energy management of hybrid photovoltaic/battery/hydrogen system. *Rev. Roum. Sci. Tech.—Série Électrotechnique Énergétique* **2022**, *67*, 21–26.
27. Uribe, J.; Santillan, E.; Camacho, O.; Ocampo-Martinez, C.; Aguirre, O. Sliding mode control approach for H_2 purity regulation in high-pressure alkaline electrolyzers. *IFAC-PapersOnLine* **2024**, *58*, 424–429. [CrossRef]
28. Roy, T.K.; Oo, A.M.T.; Ghosh, S.K. Designing a high-order sliding mode controller for photovoltaic- and battery energy storage system-based DC microgrids with ANN-MPPT. *Energies* **2024**, *17*, 532. [CrossRef]
29. Satheesan, J.; Thankappan Nair, R. An adaptive two-level hierarchical controller for universal power sharing and performance enhancement of hybrid energy storage-supported AC/DC microgrids. *Int. J. Circuit Theory Appl.* **2023**, *51*, 2122–2140. [CrossRef]
30. Singh, A.R.; Kumar, R.S.; Bajaj, M.; Khadse, C.B.; Zaitsev, I. Machine learning-based energy management and power forecasting in grid-connected microgrids with multiple distributed energy sources. *Sci. Rep.* **2024**, *14*, 19207. [CrossRef] [PubMed]
31. Csizmadia, M.; Kuczmann, M.; Orosz, T. A novel control scheme based on exact feedback linearization achieving robust constant voltage for boost converter. *Electronics* **2022**, *12*, 57. [CrossRef]
32. Ortega, R.; Van Der Schaft, A.; Maschke, B.; Escobar, G. Interconnection and damping assignment passivity-based control of port-controlled Hamiltonian systems. *Automatica* **2002**, *38*, 585–596. [CrossRef]
33. Abdolmaleki, B.; Bergna-Diaz, G. Distributed control and optimization of DC microgrids: A port-Hamiltonian approach. *IEEE Access* **2022**, *10*, 64222–64233. [CrossRef]
34. Álvarez-Arroyo, C.; Vergine, S.; De La Nieta, A.S.; Alvarado-Barrios, L.; D'Amico, G. Optimising microgrid energy management: Leveraging flexible storage systems and full integration of renewable energy sources. *Renew. Energy* **2024**, *229*, 120701. [CrossRef]
35. Thaler, B.; Posch, S.; Wimmer, A.; Pirker, G. Hybrid model predictive control of renewable microgrids and seasonal hydrogen storage. *Int. J. Hydrogen Energy* **2023**, *48*, 38125–38142. [CrossRef]
36. Hossain, M.A.; Islam, M.R.; Hossain, M.A.; Hossain, M. Control strategy review for hydrogen-renewable energy power system. *J. Energy Storage* **2023**, *72*, 108170. [CrossRef]
37. Sánchez-Squella, A.; Flores, R.; Burgos, R.; Morales, F.; Nader, A.; Valdivia-Lefort, P. 99.6% efficiency DC-DC coupling for green hydrogen production using PEM electrolyzer, photovoltaic generation and battery storage operating in an off-grid area. *Renew. Energy* **2024**, *237*, 121781. [CrossRef]
38. Villalva, M.G.; Gazoli, J.R.; Ruppert Filho, E. Comprehensive approach to modeling and simulation of photovoltaic arrays. *IEEE Trans. Power Electron.* **2009**, *24*, 1198–1208. [CrossRef]
39. Femia, N.; Petrone, G.; Spagnuolo, G.; Vitelli, M. Optimization of perturb and observe maximum power point tracking method. *IEEE Trans. Power Electron.* **2005**, *20*, 963–973. [CrossRef]
40. Tremblay, O.; Dessaint, L.A. Experimental validation of a battery dynamic model for EV applications. *World Electr. Veh. J.* **2009**, *3*, 289–298. [CrossRef]
41. García-Valverde, R.; Miguel, C.; Martínez-Béjar, R.; Urbina, A. Optimized photovoltaic generator–water electrolyser coupling through a controlled DC–DC converter. *Int. J. Hydrogen Energy* **2008**, *33*, 5352–5362. [CrossRef]
42. Yodwong, B.; Guilbert, D.; Phattanasak, M.; Kaewmanee, W.; Hinaje, M.; Vitale, G. Faraday's efficiency modeling of a proton exchange membrane electrolyzer based on experimental data. *Energies* **2020**, *13*, 4792. [CrossRef]
43. Erickson, R.W.; Maksimović, D. *Fundamentals of Power Electronics*, 3rd ed.; Springer: New York, NY, USA, 2020. [CrossRef]
44. Isidori, A. *Nonlinear Control Systems*, 3rd ed.; Springer: London, UK, 1995.
45. Liu, J.; Ming, W.; Gao, F. A new control strategy for improving performance of boost DC/DC converter based on input-output feedback linearization. In *Proceedings of the 2010 8th World Congress on Intelligent Control and Automation*; IEEE: Piscataway, NJ, USA, 2010; pp. 2439–2444.
46. Hangos, K.M.; Bokor, J.; Szederkényi, G. *Analysis and Control of Nonlinear Process Systems*; Springer: London, UK, 2004.
47. Tahir, F.; Iqbal, N.; Mustafa, G. Control of a nonlinear coupled three tank system using feedback linearization. In *Proceedings of the 2009 Third International Conference on Electrical Engineering*; IEEE: Piscataway, NJ, USA, 2009; pp. 1–6.
48. Perez, F.; Iovine, A.; Damm, G.; Ribeiro, P. DC microgrid voltage stability by dynamic feedback linearization. In *Proceedings of the 2018 IEEE International Conference on Industrial Technology (ICIT)*; IEEE: Piscataway, NJ, USA, 2018; pp. 129–134.
49. Ortega, R.; García-Canseco, E. Interconnection and damping assignment passivity-based control: A survey. *Eur. J. Control* **2004**, *10*, 432–450. [CrossRef]
50. LaSalle, J.P. Stability theory and invariance principles. In *Dynamical Systems*; Cesari, L., Hale, J.K., LaSalle, J.P., Eds.; Academic Press: Cambridge, MA, USA, 1976; pp. 211–222.

51. IRENA. *Green Hydrogen Cost Reduction: Scaling up Electrolysers to Meet the 1.5 °C Climate Goal*; Technical report; International Renewable Energy Agency: Abu Dhabi, United Arab Emirates, 2020. Available online: https://www.irena.org/publications/2020/Dec/Green-hydrogen-cost-reduction (accessed on 1 October 2026).
52. BYD Company Limited. BYD Battery-Box Premium HVS & HVM Limited Warranty (Europe), V1.2. Ten-Year Product and Performance Warranty for Stationary LFP Packs of 5–22 kWh. 2021. Available online: https://www.bydbatterybox.com/downloads (accessed on 1 October 2026).
53. Davari, S.A.; Flores-Bahamonde, F.; Mousavi, M.S.; Azadi, S.; Kouro, S.; Garcia, C.; Rodriguez, J. Predictive Phase-Shift Control of Interleaved Quadratic Buck Converter as the Power Supply of the Electrolyzer in Green Hydrogen Technology. In *Proceedings of the 2024 IEEE International Conference on Power Electronics, Drives and Energy Systems (PEDES)*; IEEE: Piscataway, NJ, USA, 2024. [CrossRef]
54. Guilbert, D.; Sorbera, D.; Vitale, G. A stacked interleaved DC-DC buck converter for proton exchange membrane electrolyzer applications: Design and experimental validation. *Int. J. Hydrogen Energy* **2020**, *45*, 64–79. [CrossRef]

Disclaimer/Publisher's Note: The statements, opinions and data contained in all publications are solely those of the individual author(s) and contributor(s) and not of MDPI and/or the editor(s). MDPI and/or the editor(s) disclaim responsibility for any injury to people or property resulting from any ideas, methods, instructions or products referred to in the content.